

## Origins and Formation of Solar Wind Transients 4 – 7 August 2011. General Description of the Complex Event and Ion Charge State Evolution

D. Rodkin<sup>1</sup> · F. Goryaev<sup>1</sup> · P. Pagano<sup>2</sup> ·  
G. Gibb<sup>3</sup> · V. Slemzin<sup>1</sup> · Yu. Shugay<sup>4</sup> · I.  
Veselovsky<sup>4,5</sup> · D. H. Mackay<sup>2</sup>

© Springer ••••

### Abstract

---

✉ D. Rodkin  
rodkindg@gmail.com  
F. Goryaev  
goryaev\_farid@mail.ru  
P. Pagano  
pp25@st-andrews.ac.uk  
G. Gibb  
gordon.gibb@ed.ac.uk  
V. Slemzin  
slem@sci.lebedev.ru  
Yu. Shugay  
jshugai@srdf.sinp.msu.ru  
I. Veselovsky  
veselov@dec1.sinp.msu.ru  
D. H. Mackay  
dhm@st-andrews.ac.uk

<sup>1</sup> P.N. Lebedev Physical Institute, Moscow, Russia

<sup>2</sup> School of Mathematics and Statistics, University of St Andrews, North Haugh, St Andrews, Fife, Scotland, KY16 9SS, UK

<sup>3</sup> School of Mathematics and Statistics, University of St Andrews, North Haugh, St Andrews, Fife, Scotland, KY16 9SS, UK now at Edinburgh Parallel Computing Centre

<sup>4</sup> Skobeltsyn Institute of Nuclear Physics, Lomonosov Moscow State University, Moscow, Russia

<sup>5</sup> Space Research Institute (IKI) RAS, Moscow, Russia

We present a case study of a complex event consisting of several solar wind transients detected by ACE on 4 – 7 August 2011 which caused the geomagnetic storm with  $Dst = -115$  nT, and their supposed coronal sources - three flares and coronal mass ejections (CMEs) occurred on 2 – 4 August 2011 in AR 11261. To investigate the solar origins and formation of these transients we studied kinematic and thermodynamic properties of expanding coronal structures using the SDO/AIA EUV images and the differential emission measure (DEM) diagnostics. The Helioseismic and Magnetic Imager (HMI) magnetic field maps were used as the input data for the 3D magnetohydrodynamics (MHD) model to describe the flux rope ejection (Pagano, Mackay, and Poedts, 2013b). We characterize the early phase of a flux rope ejection in the corona, where the usual three component structure is formed, the flux rope is ejected with the velocity at about  $200 \text{ km s}^{-1}$  to the height of 186 Mm. The kinematics of the modeled CME front well agreed with the STEREO EUV measurements. Using the results of plasma diagnostics and MHD modeling, we calculated the ion charge ratios of carbon and oxygen as well as the mean charge state of iron ions of the 2 August 2011 CME taking into account the processes of heating, cooling, expansion, ionization and recombination of the expanding plasma in the corona up to the freeze-in region. By matching the calculated ion composition parameters of the CME with that measured in-situ parameters of the SW transients we estimated the probable heating rate of the CME plasma in the low corona. We also consider the similarities and discrepancies between the results of the MHD simulation and the observation of the event.

**Keywords:** MHD; Magnetic Field; Coronal Mass Ejections; Solar Wind; Models

## 1. Introduction

The key problem of the space weather forecasting is a prediction of geoeffective transient solar wind (SW) streams that are capable to cause geomagnetic storms. One of the most geoeffective SW transients are interplanetary coronal mass ejections (ICMEs) which are considered as the interplanetary manifestations of coronal mass ejections (CMEs) associated with sporadic processes of solar activity. A comprehensive review of the topics under consideration in our paper with many further references can be found in Webb and Howard (2012). ICMEs are identified in SW as significant disturbances of the interplanetary plasma by various signatures (Gosling, 1990; Zurbuchen and Richardson, 2006) that include abnormally low plasma proton temperatures, bidirectional suprathermal electron strahls (BDEs) and energetic particle flows, cosmic ray depressions and plasma composition anomalies, which differentiate this type of transient SW flows from ambient SW and quasi-stationary flows of fast SW from coronal holes.

Richardson and Cane (2010) use the following classification of ICMEs: magnetic cloud (MC): enhanced magnetic field strength  $B > 10$  nT, smooth rotation through a large angle, low proton temperatures (Klein and Burlaga, 1982), events with evidence of a rotation in the magnetic field direction, but overall, the magnetic field characteristics do not meet those of a magnetic cloud (MC-like

events), and non-magnetic cloud events (sometimes named as "Ejecta") with some MC signatures but weaker magnetic field. Properties of MCs were studied in detail (Gosling, 1990; Webb and Howard, 1994; Burlaga *et al.*, 1998; Koskinen and Huttunen, 2006; Zhang *et al.*, 2007). Yermolaev *et al.* (2014) analyzed origins of 798 moderate (with  $100\text{nT} > Dst_{min} > 50\text{nT}$ ) and strong ( $Dst_{min} > 100\text{nT}$ ) magnetic storms for the period of 1976-2000. Their analysis showed that sheath (regions between shocks and ICMEs), MC, and ejecta generated 12%, 8%, and 20% (in total, 40%) of the magnetic storms, respectively, whereas corotating interaction regions (CIRs)- only 18%. The interplanetary sources of the other 42% of the magnetic storms are indeterminate because of data gaps. So, 69% of the identified interplanetary sources of geomagnetic storms were produced by ICMEs associated with solar origins of spontaneous activity.

For the earliest prediction of ICME arrival to the Earth one needs to understand the key factors which determine formation of transient plasma flows in the corona and their propagation in the heliosphere. For prediction purposes it is also important to investigate a link between parameters of solar sources and properties of transient plasma flows. From observational point of view, typical ICME develops in the corona in 4 main stages: (1) eruption of plasma with formation and expansion of a flux rope in the corona observable by EUV telescopes up to the distance of  $1.3 \div 1.7R_{\text{sun}}$  from the solar centre; (2) appearance of a CME in the field of view of white light coronagraphs above the limb at the distances  $> 2R_{\text{sun}}$ , (3) propagation of the CME in the heliosphere, visible by wide-field coronagraphs or heliospheric imagers; (4) appearance "in situ" of an SW transient with signatures of ICME - significant deviations of the main parameters ( $V_p, n_p, T_p, B$ ) from the ambient values (Richardson and Cane, 2004, 2010). Depending on the average speed and position of the source, ICMEs reach the Earth after  $1 \div 5$  days from startup of the eruption.

CMEs are regarded as the most evident indicator of ICMEs initiation. Origins of CMEs in the solar corona can be disclosed and localized by their characteristic signatures: solar flares, flows, magnetic reconfiguration, EUV waves, jets, coronal dimmings or brightenings, filament eruptions, post-flare loop arcades revealed by continuous monitoring of solar corona by EUV imaging using well-developed methods of data processing. However, some CMEs called as "stealth CMEs" have not evident coronal signatures. During the previous Cycle 23 (1996–2005) these events constituted about 11% of all CMEs (Zhang *et al.*, 2007), their frequency increased in solar minimum to  $\sim 30\%$  (Ma *et al.*, 2010). A case-study of stealth CMEs was published by Robbrecht, Patsourakos, and Vourlidas (2009). However, stealth CMEs are typically slow, have angular widths less than  $20^\circ$  (D'Huys *et al.*, 2014) and rarely produce significant storms (Kilpua *et al.*, 2014).

CMEs are predominant during the solar activity peak, their rate increases on an order of magnitude from solar minimum ( $0.5\text{ day}^{-1}$ ) to maximum ( $> 5\text{ day}^{-1}$ ) (Gopalswamy *et al.*, 2004; Webb and Howard, 1994). Munro *et al.* (1979) reported that  $\sim 40\%$  of CMEs were associated with  $H_{\alpha}$  flares. Andrews (2003) reported that  $\sim 60\%$  of M-class flares were associated with CMEs. Yashiro and Gopalswamy (2009) examined the CME associations with the peak flux, fluence, and duration of flares for the period from 1996 to 2007 and found that the CME

association rate clearly increases with the peak flare X-ray flux from  $\sim 20\%$  for the C-class flares to more than  $90\%$  for X-class flares.

Prediction of ICMEs arrival to the Earth environment in a greater extent depends on the CME kinematics in the heliosphere. Due to the absence of regular SW measurements in the interplanetary space, currently such prediction can be provided only by using various SW propagation models. The simplest one, the Archimedean spiral (or ballistic) model (ASM), is based on the assumption that SW transients remain their speed constant during the whole passage from the Sun to the Earth (Nolte and Roelof, 1973; McNeice, Elliot, and Acebal, 2011). The drag-based model (DBM) supposes that the dynamics of CMEs is dominated by the MHD aerodynamic drag (Cargill *et al.*, 1996; Vršnak, 2001; Owens and Cargill, 2004; Cargill, 2004; Vršnak *et al.*, 2004, 2010; Vršnak and Žic, 2007; Vršnak, Vrbanec, and Čalogović, 2008; Borgazzi *et al.*, 2009; Lara and Borgazzi, 2009), i.e., that above the distance of  $20 R_{\text{Sun}}$  CMEs which are faster than the ambient solar wind are decelerated, whereas those slower than solar wind are accelerated by the ambient flow (Gopalswamy *et al.*, 2000). The validation analysis showed that the mean uncertainty in predicting the arrival times of ICMEs by the DBM is from 12.9 hours, when deviation of CMEs from the Sun-Earth line is larger than their half-width, to 6.8 hours when such deviation is smaller (Vršnak *et al.*, 2013; Shi *et al.*, 2015).

Currently several sophisticated physics-based models are under development for the SW forecasting near the Earth and further with the use of the magnetohydrodynamic (MHD) approach: the Wang-Sheeley-Arge (WSA)-Enlil model, MHD-Around-a-Sphere (MAS)-Enlil model, SpaceWeather Modeling Framework (SWMF), and their combinations (Jian *et al.*, 2015). These models structurally consist of two main parts: solar coronal and heliospheric components. The coronal part of the WSA, MAS, and SWMF models approximates the outflow at the inner boundary of the heliosphere based on full-rotation synoptic magnetograms constructed from daily full-disk photospheric magnetograms (Arge and Pizzo, 2000) using the semi-empirical model based on the potential magnetic field approximation. Then, the boundary outflow and magnetic field distributions are used as the initial data in the MHD simulation which describe radial expansion and evolution of the SW plasma in the heliosphere. These models were initially designed for predicting propagation of the ambient SW or quasi-stationary large-scale SW structures like high-speed flows from coronal holes or stream interface regions. For forecasting propagation of SW transients the models use additional information from coronagraphs about parameters of a CME at the boundary between the corona and heliosphere.

The Enlil model is a 3-D time-dependent heliospheric model based on the ideal MHD equations (Odstrčil, 1994; Odstrčil, Dryer, and Smith, 1996; Odstrčil and Pizzo, 1999). The inner boundary of Enlil model is placed at  $21.5$  or  $30 R_{\text{sun}}$  beyond the outermost critical point, and the outer boundary is taken from  $2$  to  $5$  or  $10$  AU. To predict propagation of CMEs, the WSA-Enlil cone model additionally uses white-light images from Large Angle and Spectrometric Coronagraph LASCO (Brueckner *et al.*, 1995) and coronagraphs aboard the Solar Terrestrial Relations Observatory STEREO (Howard *et al.*, 2008). Such model which characterize the basic properties of a CME, including speed, direction

and size (Pizzo *et al.*, 2011; Mays *et al.*, 2015). Principally, this model focuses on prediction of arrival time of a CME without localization of its coronal origin. Mays *et al.* (2015) in their statistical analysis of 35 CMEs occurred between January 2013 and July 2014 concluded that the mean estimation error of the CME arrival by the ENLIL model was 12.3 hours. Inaccuracy of the current models to a considerable degree arises from insufficient knowledge of interaction of the CME plasma with the ambient SW and other SW components in the heliosphere. Information about these processes can be obtained from the fast progressing heliospheric tomography based on the interplanetary scintillation (IPS) in radio waves (Manoharan, 2010).

Among other parameters of the SW transients, the ion charge composition of the SW plasma is one of the important identifiers of their origin, whereas it depends on the parameters of the source and remains practically unchanged during the SW propagation in the heliosphere (Fisk, Schwadron, and Zurbuchen, 1998; Zhao, Zurbuchen, and Fisk, 2009; Zhao *et al.*, 2014; Kilpua *et al.*, 2014; Wang, 2012). Analysis of the ion charge state and mass composition of the SW plasma helps to separate different components of SW and to determine their sources. For example, such characteristics as: increased charge state of oxygen ions and iron, abundance of elements with a low ionization potential compared with that in the photosphere suggests that the SW transient originated from hot coronal source with closed configuration of the magnetic field.

It is believed that the ion charge state of SW, registered at the Earth orbit, approximately corresponds to its state in the corona at the altitude where it is "freezed-in" (a transition to the limiting case where the ionization and recombination times of plasma in the corona are of order or larger than the time of SW propagation in the heliosphere (Hundhausen, Gilbert, and Bame, 1968)). Freeze-in occurs at distances between 1.5 to  $4R_{\text{sun}}$ , which depends on the type of ion, and the level of activity (Feldman, Landi, and Schwadron, 2005). For comparison, other parameters of the SW transients, such as velocity and magnetic field strength, can vary considerably in the heliosphere due to interaction of transient flow with the quasi-stationary ambient and high-speed SW components.

The problem of identification and localization of solar wind sources is one of the actual challenges in solar physics. One of the important sources of information used for this purpose is in-situ measurements of ion charge state of solar wind plasma near the Earth. However, ion charge state of SW plasma near the Earth characterizes plasma properties in the freeze-in region, and not in the source on the solar surface. Therefore, actual is also the problem of the evolution of CME plasma parameters propagating from the source to the freeze-in region.

The main factors that determine the ion composition of the outflow plasma and its evolution in the corona are temperature, density, and mass velocity which depend on the level of solar activity: at higher activity, plasma temperature and density in the source and the average CME velocity increase. During expansion of the outflow plasma from the origin to the freeze-in region its ion composition evolves due to various processes, such as heating by energy release from the flare site and cooling by the heat conduction, radiation losses, the adiabatic expansion. These processes influence on the plasma temperature, or more exactly, on the energy distribution of its electron component which governs a balance between

ionization and recombination and defines the ion composition of an ejecta. From in-situ measurements it was established that the faster CME/ICMEs as a rule have higher ion charge states in comparison with the slower ones, probably, due to deeper cooling of the outflow plasma during its longer passage through the corona (Gopalswamy *et al.*, 2013).

Gruesbeck *et al.* (2011) presented a procedure for deriving the ion composition of CMEs in the corona. To achieve this, they used in-situ measurements of ion charge states of C, O, Si, and Fe and interpreted them in the context of a model for the early evolution of the CME plasma. They obtained, in particular, the best fit for the data, which was provided by an initial heating of the plasma, followed then by an cooling expansion. Gruesbeck *et al.* (2011) pointed out important constraints for the heating and expansion timescales, as well as the maximum temperature of the CME plasma during its eruption. Lepri *et al.* (2012) presented an analysis and comparison of the heavy ion composition observed during the passage of the ICME at L1 and at Ulysses. They compared the ion composition obtained across the two different observation cuts through the ICME with predictions for heating during the eruption based on models of the time-dependent ionization balance throughout the event. The authors of the both papers based their considerations only on assumptions about conditions in the coronal sources not comparing them with measurements.

Lynch *et al.* (2011) and then Reinard, Lynch, and Mulligan (2012) use large scale non ideal 2.5D MHD simulations of the solar wind and investigate the ion charge state composition during a CME by tracking in post process a grid of Lagrangian plasma parcels. In Reinard, Lynch, and Mulligan (2012) they find only a qualitative matching between the observation and model in the charge state enhancements in the flux rope material and in the front, while in Lynch *et al.* (2011) is explained that they cannot obtain a quantitative matching with observations because only a fully 3D model is essential to properly describe the ionization state of plasma elements. The 3D MHD model presented here (Pagano, Mackay, and Poedts, 2013b) certainly addresses these improvements, however the very different spatial domains of the two studies make difficult a direct comparison. Pagano *et al.* (2008) already had sucessfully experimented to derive the ion composition from the post-processing of MHD simulations, where they explained several observational features of shocks connected to CMEs by reconstructing the out of equilibrium ionization state of O VI and Si XII when an MHD shock invests the plasma.

In our work we describe a complex method of predicting ion composition of SW transients using both numerical simulation and direct observations of the CME initiation in the corona. Such method enables to establish relations between parameters of the CME origins in the corona and the resulting parameters of SW transients which can be used further for improving the SW forecasting methods. We consider a case of three X-ray flares and CMEs in the corona occurred on 2 – 4 August 2011, which led to significant disturbances of SW near Earth on 4 – 7 August 2011 producing a strong magnetic storm with a minimum value of  $Dst = -115$  nT. The August storm and its modeling with the main attention to the NS asymmetry on the Earth was considered in Yiğit *et al.* (2016). In our work we focus on the solar part of this complex event, which

is favorable for investigation because the associated coronal phenomena were observed near the solar disk center, and the resulting CMEs were seen by the Sun Earth Connection Coronal and Heliospheric Investigation (SECCHI) (Howard *et al.*, 2008) instruments aboard STEREO-A and B spacecraft in quadrature. For the analysis we used the data from the Solar dynamic Observatory (SDO): solar EUV images from the Atmospheric Imaging Assembly (AIA) telescope (Lemen *et al.*, 2012) and the photospheric magnetic field maps from the Heliospheric and Magnetic Imager (HMI) instrument (Schou *et al.*, 2012). Diagnostics of flares in the coronal sources were made using the GOES X-ray data, parameters of the outflow plasma were defined by the differential emission measure (DEM) method using the AIA multi-wavelength EUV images. Using the magnetic field maps, we simulated a formation of a flux rope by the ideal 3D MHD model and compared the results with the data obtained from measurements. The results of modeling and plasma diagnostics were used for calculation of ion composition of the erupting plasma taking into account its evolution in the solar corona. The calculated charge states of carbon, oxygen and iron ions were compared with measurements in-situ by Advanced Composition Explorer (ACE, Stone *et al.* (1998)). In the Discussion and Summary sections we consider different factors which influence on reliability and accuracy of predicted parameters of ICMEs. In Section 2 of the current paper we describe the observational data for all three solar events, in the following sections we consider in detail the first event occurred on 2 August 2011. A special case of the events of 3 and 4 August, when the two CMEs interacted in the heliosphere, will be considered in the next publication.

This work was fulfilled as a contribution to the International Study of Earth-affecting Solar Transients (ISEST)/ Minimax 24 project (the event of 4 August 2011 is included into the ISEST event list<sup>1</sup>.

## 2. SW transients of 4 – 7 August 2011 and their solar origins

Figure 1 shows the Level 2 1 hour-averaged ACE SW data for the period from 4 to 8 August 2011. The SW transients identified in these data were referenced in three ISEST-related databases. The ICME/CME lists of George Mason University (GMU)<sup>2</sup> and University of Science and Technology of China (USTC)<sup>3</sup> describe only one ICME of 6 August 2011 classified as the MC+SH event (GMU list) or SH+EJ event (USTC list) which led to the geomagnetic storm of 6 August, 12:00 UT, with  $Dst = -115$  nT. The GMU list associates ICME with the M9 flare and Halo CME occurred on 4 August 2011. The Richardson and Cane ICME list (hereafter R&C list)<sup>4</sup> refer two shocks and two ICMEs indicated in Table 1 and marked in Fig. 1. The first ICME showed small enhancements of magnetic field, proton density and velocity above the background level. The

---

<sup>1</sup>[http://solar.gmu.edu/heliophysics/index.php/The\\_ISEST\\_Event\\_List](http://solar.gmu.edu/heliophysics/index.php/The_ISEST_Event_List)

<sup>2</sup>[http://solar.gmu.edu/heliophysics/index.php/GMU\\_CME/ICME\\_List](http://solar.gmu.edu/heliophysics/index.php/GMU_CME/ICME_List)

<sup>3</sup>[http://space.ustc.edu.cn/dreams/wind\\_icmes](http://space.ustc.edu.cn/dreams/wind_icmes)

<sup>4</sup><http://www.srl.caltech.edu/ACE/ASC/DATA/level3/icmetable2.htm>

temperature-related ion ratios  $C^6/C^5$ ,  $O^7/O^6$  and the mean charge of iron ions QFe slightly exceeded the background. Only the structure-related Fe/O ratio showed a noticeable increase to the value of 0.55, which corresponds to the FIP-bias  $\sim 3$  and evidences a presence of plasma from closed magnetic structures in the source. The second ICME displayed a jump of the proton velocity to 610 km but moderate enhancements of magnetic field magnitude and proton density. Thus, the typical ICME signatures (Zurbuchen and Richardson, 2006; Richardson and Cane, 2004), except the decreased proton temperature and the ion composition, were slightly expressed for both ICMEs. The negative values of  $B_z$  component of IMF (-5 and -17 nT in the GSM coordinate system) were registered in the sheaths followed the shocks before the ICMEs, being the most likely cause of the geomagnetic storm of 6 August 2011. The development of this storm was considered in detail by Yiğit *et al.* (2016).

Application of the ballistic propagation model (assuming a constant ICME speed between the Sun and the Earth) gives the following transit times and the time slots (hereafter all times are in UT) for the solar events produced these ICMEs (with uncertainty  $\pm 12$  hours): for ICME 1  $t_{transit} = 63$  hours, the source time slot is from 1 August 2011, 18:57 to 2 August 2011, 18:57, for ICME 2 – 38 hours, the time slot is from 3 August 2011, 15:31, to 4 August 2011, 15:31. During these time slots, 3 flares and 3 CMEs occurred in AR 11261 (Table 2). In order to identify the solar origins of the SW transients, we used two heliospheric CME propagation models: the Advanced Drag Model(ADM) (Vršnak *et al.*, 2013) and the WSA-Enlil Model (Pizzo *et al.*, 2011). For three CMEs listed in Table 2 taking the asymptotic SW velocity equal  $350 \text{ km s}^{-1}$  ADM gives the transit times 64, 60 and 51 h with the mean uncertainty  $\sim 10$  h (Shi *et al.*, 2015), which corresponds to the time slots of the coronal source initiation time 3 August 2011, 12:02 – 5 August 2011, 08:02 UT, 5 August 2011, 15:42 – 6 August 2011, 11:42 and 5 August 2011, 21:36 – 6 August 2011, 17:36. These time slots are well agree with the three SW transients seen in the ion charge state data (Figure 2) with the mean difference of 6.5 hours. The mean and maximum values of the ion composition parameters for these SW transients are given in Table 3.

The question arises, why the three CMEs produced three SW transients in the ion composition data, but only two ICMEs have been identified by other signatures. To find the answer, we consider the results of simulation of this complex event by the WSA-Enlil model presented in the Enlil SW prediction Helioweather database<sup>5</sup>. It was found that due to higher velocity the SW transient associated with the CME 3 (started on 4 August 2011) overtook that from CME 2 (started on 3 August 2011) at the distance of  $\sim 0.6$  AU when the first transient already reached the Earth. In Figure 3 are presented the normalized density in the ecliptic plane for 5 August 2011 and the J-map for all three SW transients from the Helioweather database. As a result of interaction between the second and third transients, the merged cloud reached the Earth between 5 August 2011, 14:00 and 7 August 2011, 00:00 producing the observed variation of the ion composition.

<sup>5</sup><http://helioweather.net/archive/2011/08/>

**Table 1.** Data on ICMEs of 4 – 5 August 2011 presented in the Richardson and Cane ICME list (<http://www.srl.caltech.edu/ACE/ASC/DATA/level3/icmetable2.htm>)

N of event	Shock date/time	ICME start date/time	ICME end date/time	$V_{max}$ $\text{km s}^{-1}$	$V_{transit}$ $\text{km s}^{-1}$
1	2011 Aug. 4 21:53	2011 Aug. 5 05:00	2011 Aug. 5 14:00	440	430
2	2011 Aug. 5 17:51	2011 Aug. 6 22:00	2011 Aug. 7 22:00	610	540

**Table 2.** Flares and CMEs occurred on 2 – 4 August 2011

Date of event	Flare onset time	Flare class	CME (STA) onset time	$V_{CME}$ $\text{km s}^{-1}$	CME (LASCO) onset time	$V_{CME}$ $\text{km s}^{-1}$
2011 Aug. 2	05:19	M1	05:54	781	06:36	712
2011 Aug. 3	13:24	M6	13:54	892	14:00	610
2011 Aug. 4	03:41	M9	04:12	1193	04:12	1315

In the following sections we consider in general the complex SW event of 4 – 7 August 2011, its coronal sources and in detail – formation of the first transient associated with CME 1 of 2 August 2011. The features of the second and third transients and their relations with the solar origins will be considered in further publications.

### 3. Formation of the CME of 2 August 2011 in the corona

#### 3.1. Kinematics

We studied formation of three CMEs of 2–4 August 2011 in the low corona using the SDO/AIA images in different wavelength channels. After preliminary

**Table 3.** Ion composition parameters of solar wind transients

N of SW tr.	start fin	$C^6/C^5$ min/max/mean	$O^7/O^6$ min/max/mean	$Q_{Fe}$ min/max/mean	Fe/O min/max/mean
1	Aug. 4 21:00 Aug. 5 14:00	0.74/3.40/1.75	0.11/0.40/0.26	9.28/11.5/10.2	0.13/0.55/0.29
2	Aug. 5 17:51 Aug. 6 06:00	0.70/5.01/2.30	0.22/1.19/0.54	10.4/14.0/11.6	0.12/0.37/0.19
3	Aug. 6 06:00 Aug. 6 22:00	0.61/5.46/2.55	0.11/1.32/0.60	10.6/15.9/13.2	0.14/0.52/0.32

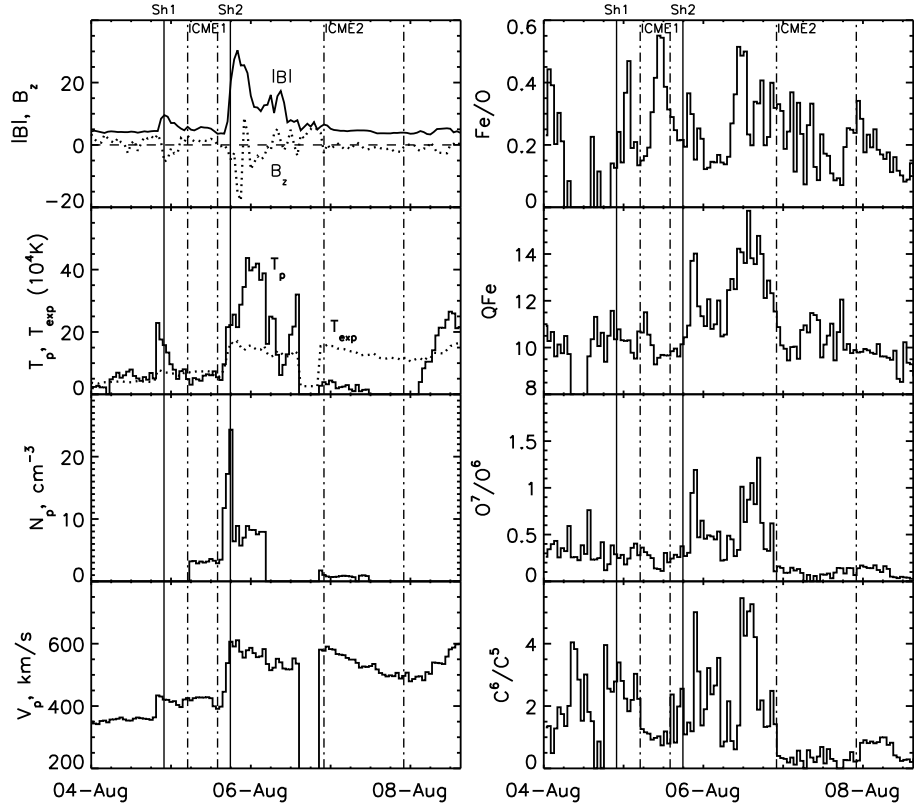


**Figure 1.** ACE solar wind data for 4–8 August 2011. The times of shocks Sh1 and Sh2 are marked by the solid lines. The start and end of interplanetary coronal mass ejections CME 1 and CME 2 are marked by dot-dashed lines.

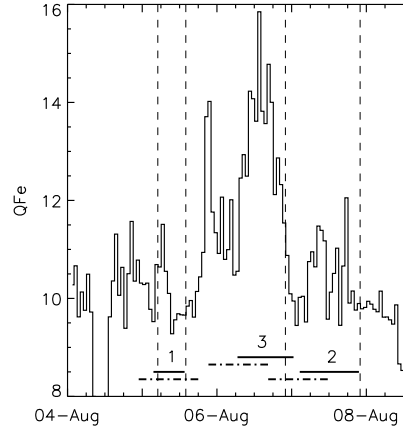


**Figure 2.** The ACE  $Q_{Fe}$  data and appearance time slots of the solar wind transients associated with the CMEs of 2–4 August 2011 obtained with ADM. Solar wind transients identified from the ion charge state enhancements are marked by the dashed lines.

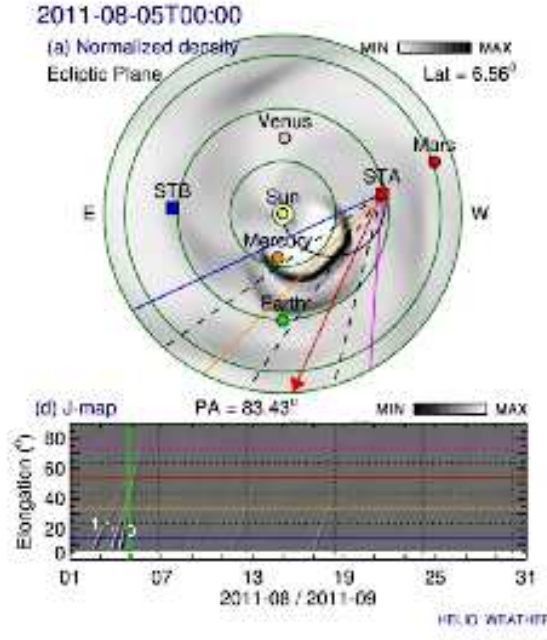


**Figure 3.** The normalized density in the ecliptic plane and the J-map for all three solar wind transients obtained with the WSA-Enlil model (<http://heliowebster.net/archive/2011/08/>)

processing the data from Level 1 to Level 1.5 we produced running-difference images to disclose the moving coronal structures associated with a CME. These structures are seen as expanding loops but in fact they represent projections of the expanding erupting magnetic shells integrated over their legs along the line-of-sight (LOS). In the studied events the largest contrast reached in the 211 Å channel images.

Figure 4a represents a group of expanding loop-like structures in the 211 Å running-difference image at 05:58:02, 2 August 2011, in the initial stage of the CME 1 formation (Table 1). These structures apparently represent projections of the eruption shell to the disk plane. They disappeared at  $\sim 06:00$ , probably, due to the CME take-off and not likely by heating, as it will be shown in the next section. The distance-time graphs in Figure 4b show elevation of the CME in the low corona seen by the EUV AIA images (channel 211 Å), above the limb seen by STEREO-A/EUVI in 171 Å (Fig. 4c) and in the field of view of the LASCO C2 coronagraph. We converted transverse distances into height assuming that vertical  $d_r$  and horizontal  $d_h$  displacements are in the same relation as the radial velocity of the CME  $v_r$  measured by STEREO-A/Cor2 and transversal velocity  $v_h$  measured by LASCO:  $d_r/d_h \simeq v_r/v_h = 1.09$ . Fig. 4d shows the dependence of the CME radial velocity with height calculated from the data of different instruments. During expansion, the CME velocity increased from  $26 \text{ km s}^{-1}$  at  $h_r \simeq 0.06 R_{\text{sun}}$  to  $\sim 800 \text{ km s}^{-1}$  at  $5R_{\text{sun}}$ .

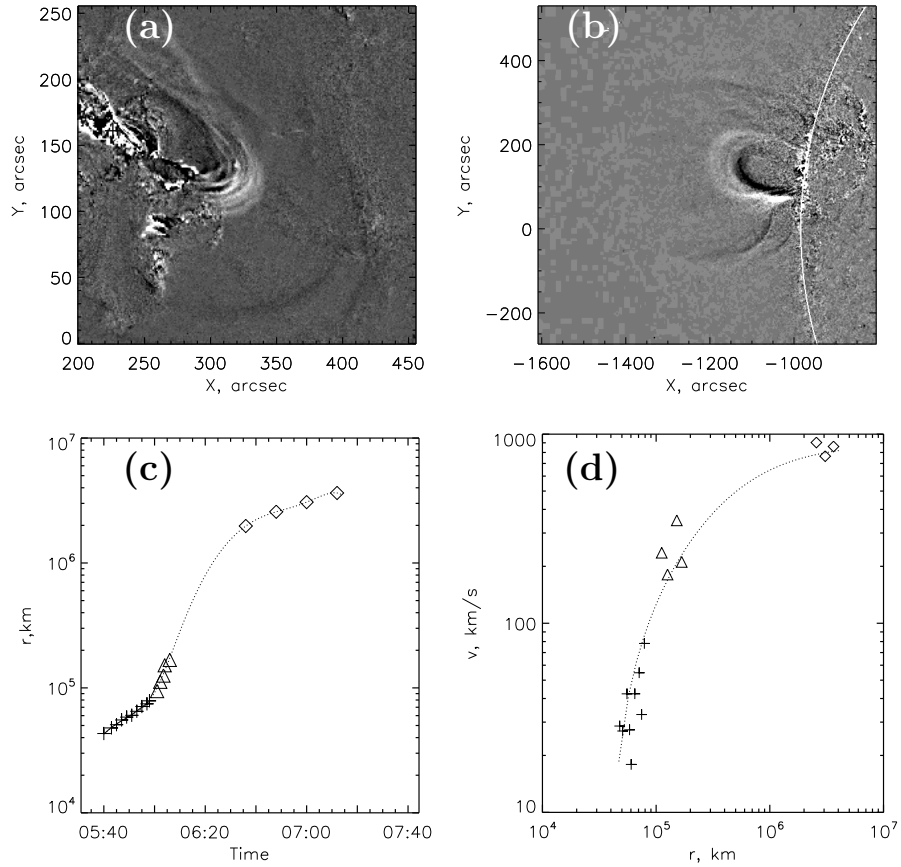


**Figure 4.** Formation of the CME on 2 August 2011. (a) The running difference image (AIA, 211 Å) shows the eruption structures in projection to the disk at 05:58:02. (c) Dependence of the CME expansion height (the origin is marked by the cross in Fig. 4a) with time. Crosses correspond to the brightest structure at the disk seen by AIA, triangles - to the CME expansion above the limb seen by STEREO-A/EUVI, squares - to the CME expansion seen by LASCO/C2. (b) The running-difference image of the CME seen by STEREO-A/EUVI in 171 Å at 06:02:15. (d) Dependence of the CME radial velocity on time seen by AIA, EUVI and LASCO (symbols are the same as in (c)). The dotted line shows the fitting function (see in the text).

### 3.2. Plasma diagnostics

For deriving plasma parameters from the observed spectral data, we carried out plasma diagnostics for both flares and CME plasmas. We used the differential emission measure (DEM) analysis to derive averaged plasma parameters such as electron temperatures and densities of plasma structures under consideration. The DEM analysis was carried out using intensities in six AIA/SDO EUV lines: 94 Å, 131 Å, 171 Å, 193 Å, 211 Å, and 335 Å. In several points along the direction of propagation we built the light curves of the mean intensities in the

**Table 4.** Averaged values of electron temperature and density in the flare on 2 August 2011.

Time	$T_{\text{eff}}$ , MK	$n_e$ , cm $^{-3}$
05:32	9.12	1.53e9
05:44	7.31	2.48e9
05:50	7.19	2.40e9

4x4 pixel boxes as a function of time and determined the fluxes in each line as the maximal value minus the mean background. The intensity flux  $F_i$  in the line  $i$  can be written as

$$F_i = \int_{\Delta T} G_i(T) DEM(T) dT, \quad (1)$$

where  $G_i(T)$  is the temperature response function of the passband  $i$ , and  $DEM(T)$  is the DEM distribution of plasma. To retrieve the function  $DEM(T)$ , we have made use of a DEM technique based on a probabilistic approach to the inverse problem (see, e.g., (Urnov *et al.*, 2007; Goryaev *et al.*, 2010; Urnov, Goryaev, and Oparin, 2012) for the details). A DEM temperature distribution for each plasma structure under consideration was then used to determine an effective temperature,  $T_{\text{eff}}$ , according to the formula

$$T_{\text{eff}} = \frac{\int_{\Delta T} T G(T) DEM(T) dT}{\int_{\Delta T} G(T) DEM(T) dT}, \quad (2)$$

where  $G(T) = \sum_i G_i(T)$  is the total temperature response for all lines. The averaged electron density in a given plasma structure was then estimated using the total emission measure (EM) and plausible geometry of the corresponding plasma structure.

The values of averaged temperatures and densities for the flare on 2 August 2011 are given in Table 4. Furthermore, the plasma parameters for the moving CME plasma structure under study on 2 August 2011 in the range of altitudes of about  $0.1\text{--}0.15 R_{\text{sun}}$  from the solar surface are presented in Figure 5. It is worth noting that the temperatures in the moving plasma structures are noticeably lower than in the corresponding flares.

#### 4. Numerical simulation of the flux rope ejection

To model this specific flux rope ejection in the solar corona, we use an ideal 3D MHD simulation coupled with a continuous time series evolution of the magnetic field through a series of quasi-static Non-Linear Force-Free (NLFF) fields. The

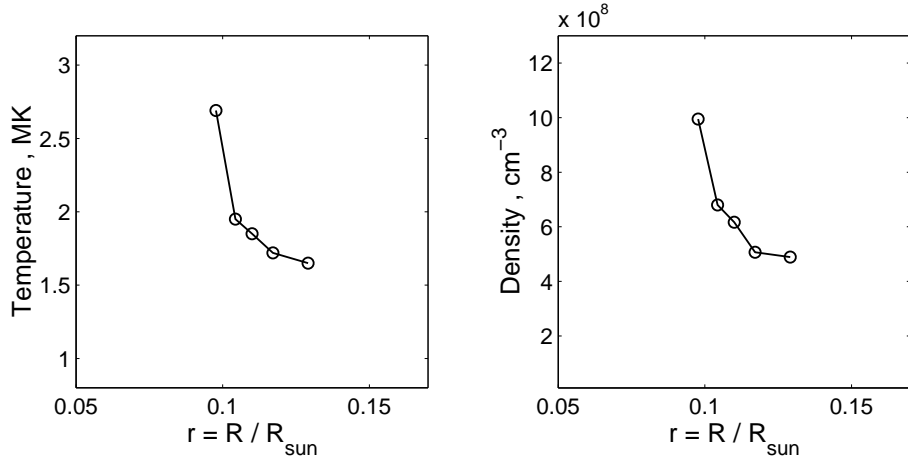


**Figure 5.** Electron temperature and density evolution for the expanding plasma structure determined by the DEM method from the AIA images on 2 August 2011.

later technique is used to produce a non-potential initial condition that is used in the ideal MHD simulation. This approach is a combination of the models presented in Pagano, Mackay, and Poedts (2013b) and Gibb *et al.* (2014) that has been specifically tuned for the present simulation.

The key idea is to describe the flux rope formation and the conditions prior to the onset of the ejection with the time series of NLFF fields, suited for a slow, quasi-static, and magnetically dominated evolution and to adopt a full MHD description for when the evolution of the system becomes fast, out of equilibrium and in a multi- $\beta$  regime.

#### 4.1. NLFF Time Series

In order to describe the slow evolution of the region of interest, a continuous time series of NLFF fields is generated from the corresponding time series of magnetograms (Mackay, Green, and van Ballegooijen, 2011; Gibb *et al.*, 2014). In the present application we use 50 magnetograms from 31 July 2011 at 05:00:41 to 2 August 2011 at 06:00:41 sampled every 60 minutes. The procedure and set of equations solved is the same as in Mackay, Green, and van Ballegooijen (2011).

The time series of NLFF fields are constructed assuming 4 closed boundaries at the sides for the 3D box. The bottom boundary representing the solar surface is forced to have magnetic flux balance and the top boundary is set to be open.

In Fig.6a-b we show the initial magnetogram image on 31 July 2011 at 05:00:41 and the final magnetogram image on 2 August 2011 at 06:00:41 with the final 3D magnetic configuration shown by the green lines. The initial magnetic configuration is assumed to be potential, while the final stage is highly non potential with a magnetic flux rope formed. Over the time series of NLFF fields a magnetic flux rope forms as a consequence of the continuous motion and evolution of the magnetic field at the lower boundary. The flux rope forms along the polar inversion line (PIL) and is about  $2 \times 10^9$  cm long and its centre

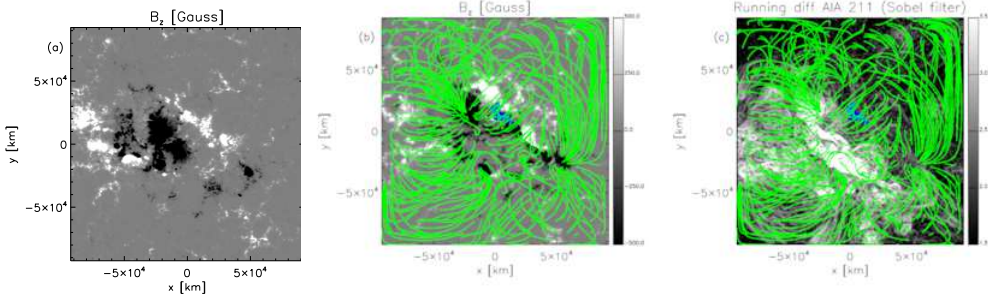


**Figure 6.** Maps of the surface magnetic field measured by the magnetograms on 31 July 2011 at 05:00:41 (a) and on 2 August 2011 at 06:00:41 (b). In (b) we over plot some magnetic field line from the 3D magnetic configuration obtained with the NLFFF time series. Blue lines are representative of the flux rope; (c) maps of running differences images from AIA 211Å filter with applied Sobel filter and overplotted magnetic field lines.

is located at the coordinates  $x = 5.44 \times 10^8$  cm and  $y = 1.27 \times 10^9$  cm. The flux rope covers only part of the PIL, whereas sheared magnetic field lines are present along the whole PIL, marking the non potentiality of the final magnetic field configuration.

Fig.6c shows a running difference of AIA 211Å pass band image at the same time of the last magnetogram where we apply the sobel filter. The sobel filter highlights structures and allows a comparison with the overplotted magnetic field lines to assess the quality of the reconstruction from the NLFF time series. We find that the general topology of the loops is reproduced where the magnetic field lines match i) the loop structures at the left-lower corner of the image, ii) the system of loops departing in different directions from the enhanced emission region and iii) many of the loops around the magnetic flux rope.

It is also crucial to point out that due to slow variation of the magnetic field, the final magnetic configuration is not sensitive to time intervals of some minutes in comparison with 60 minutes sampling time of the HMI magnetograms. This means that the final configuration could represent any time within some minutes around the exact magnetogram used.

#### 4.2. MHD Model

The final 3D magnetic configuration from the NLFF time series is then used as input for an ideal MHD simulation. This approach is an extension of the technique successfully adopted in Pagano, Mackay, and Poedts (2013b) and then further developed in Pagano, Mackay, and Poedts (2013a) and Pagano, Mackay, and Poedts (2014), where the magnetic configuration obtained from a magneto-frictional non-linear force-free model is input as initial condition in an ideal MHD simulation.

In order to do so, we import the three components of the magnetic field from the NLFF time series grid to the grid of our 3D MHD model. Specifically in

Pagano, Mackay, and Poedts (2013b) and Pagano, Mackay, and Poedts (2013a) there are a number of thorough tests to show that this is possible such that we preserve the stability or instability of the configuration.

#### 4.2.1. Interpolation of the magnetic configuration

In the present paper we have simplified the way in which the 3D interpolation is performed and have adopted a cartesian grid. In cartesian coordinates, let  $B(x, y, z)$  be the value that we want to compute in the position  $(x, y, z)$  that we know lies in the cell defined by the indexes  $[i : i + 1, j : j + 1, k : k + 1]$  where the quantity  $b$  is defined. We compute

$$B(x, y, z) = \sum_{i,j,k}^{i+1,j+1,k+1} b[i, j, k] V[i, j, k] / V \quad (3)$$

where  $V[i, j, k]$  is the volume defined by the point  $(x, y, z)$  and the cell corner opposite to the position  $[i, j, k]$  and  $V$  is the sum of these volumes. This approach guarantees the continuity of the solution and its smoothness independently of the spatial resolution of the grid where  $B(x, y, z)$  is defined.

#### 4.2.2. Plasma distribution

As the time series of NLFF fields provides only the magnetic configuration, we need to adopt an initial distribution of plasma density, velocity and temperature in order to close a complete set of MHD variables. We aim at a realistic and general representation of the solar corona, so we seek to produce a distribution of plasma that takes into account the heterogeneity of the coronal plasma. In particular we intend to describe the flux rope plasma as colder and denser than the plasma outside of the flux rope. Magnetic flux ropes are structures where the magnetic field is usually more intense than their surroundings and where the magnetic field presents a twist. Therefore, we define the following proxy function to link the plasma temperature and density to the magnetic field:

$$\omega = \sqrt{\omega_x^2 + \omega_y^2 + \omega_z^2} \quad (4)$$

where

$$\omega_x = \frac{|\mathbf{B} \times \nabla B_x|^2}{|\nabla B_x|^2} \quad (5)$$

$$\omega_y = \frac{|\mathbf{B} \times \nabla B_y|^2}{|\nabla B_y|^2} \quad (6)$$

$$\omega_z = \frac{|\mathbf{B} \times \nabla B_z|^2}{|\nabla B_z|^2} \quad (7)$$

where  $\mathbf{B} = (B_x, B_y, B_z)$  is the magnetic field, the cartesian coordinates  $x, y$  are tangent to the solar surface and  $z$  is perpendicular to the surface. The function  $\omega$  is positive definite and peaks where the magnetic field presents more twisting and is more intense, e.g. near the centre of the magnetic flux rope axis. As an example, at the flux rope axis  $\nabla B_z$  is parallel to the solar surface along the direction connecting two opposite polarities and perpendicular to the magnetic field that is mostly parallel to the  $x-y$  plane. In this configuration  $\omega_z$  is relatively high. Additionally, the value of  $\omega$  is proportional to the magnetic field intensity, which results in it being higher near the solar surface and lower at further radial distances from the solar surface.

In order to effectively use  $\omega$  to model the solar atmosphere we define the function:

$$\Omega = \arctan \frac{\omega - \omega^*}{\Delta\omega} / \pi + 0.5 \quad (8)$$

where  $\omega^*$  and  $\Delta\omega$  are two simulation parameters.  $\Omega$  is then bound between 0 and 1 and the temperature is defined by:

$$T = \Omega(T_{fluxrope} - T_{corona}) + T_{corona} \quad (9)$$

where  $T_{fluxrope}$  and  $T_{corona}$  are two simulation parameters that respectively represent the temperature in the flux rope and in the external corona. The thermal pressure is independently specified by the exponential solution for hydrostatic equilibrium with constant gravity with a uniform temperature set equal to  $T_{corona}$ :

$$p = \frac{\rho_0}{\mu m_p} k_B T_{corona} \exp\left(-z \frac{g \mu m_p}{k_B T_{corona}}\right) \quad (10)$$

where  $p$  is the thermal pressure,  $\rho_0$  is a simulation parameter that sets the density at the solar surface,  $\mu = 1.31$  is the average particle mass,  $m_p$  is the proton mass,  $k_B$  is the Boltzmann constant and  $g$  is the solar gravitational acceleration at the solar surface. The density  $\rho$  is given by the equation of state:

$$\rho = \frac{p}{T(\mathbf{B})} \frac{\mu m_p}{k_B} \quad (11)$$

where  $\rho$  is the density,  $T$  is the temperature.

#### 4.2.3. MHD simulation

Based on the approach described in Sec.4.2.2 and using the final 3D magnetic field configuration obtained from the NLFF time series as described in Sec.4.1, we construct the initial condition for the MHD simulation, where Table 5 shows the value used in our model for the relevant parameters.

We use the MPI-AMRVAC software (Porth *et al.*, 2014), to solve the MHD equations where external gravity is included as a source term,

$$\frac{\partial \rho}{\partial t} + \nabla \cdot (\rho \mathbf{v}) = 0, \quad (12)$$

**Table 5.** Parameters for the initial condition of the ideal MHD Simulation

Parameter	value	Units
$\rho_0$	$1.1 \times 10^{-12}$	$g/cm^3$
$\omega^*$	300	$G$
$\Delta\omega$	80	$G$
$T_{fluxrope}$	$10^5$	K
$T_{corona}$	$2 \times 10^6$	K

$$\frac{\partial \rho \mathbf{v}}{\partial t} + \nabla \cdot (\rho \mathbf{v} \mathbf{v}) + \nabla p - \frac{(\nabla \times \mathbf{B}) \times \mathbf{B}}{4\pi} = \rho \mathbf{g}, \quad (13)$$

$$\frac{\partial \mathbf{B}}{\partial t} - \nabla \times (\mathbf{v} \times \mathbf{B}) = 0, \quad (14)$$

$$\frac{\partial e}{\partial t} + \nabla \cdot [(e + p)\mathbf{v}] = \rho \mathbf{g} \cdot \mathbf{v}, \quad (15)$$

where  $t$  is time,  $\mathbf{v}$  velocity,  $\mathbf{g}$  is the vector of the solar gravitational acceleration, and the total energy density  $e$  is given by

$$e = \frac{p}{\gamma - 1} + \frac{1}{2} \rho \mathbf{v}^2 + \frac{\mathbf{B}^2}{8\pi}, \quad (16)$$

where  $\gamma = 5/3$  denotes the ratio of specific heats.

The computational domain is composed of  $256 \times 256 \times 248$  cells, distributed on a uniform grid. The simulation domain is similar to the one used in the time series of NLFF fields and it extends over  $1.86 \times 10^5$  km in the  $x$  and  $y$  direction and over  $1.85 \times 10^5$  km in the  $z$  direction starting from  $z = 1.86 \times 10^3$  km above the photosphere. The boundary conditions are treated with a system of ghost cells. Two layers of cells between  $z = 0$  and  $z = 1.49 \times 10^3$  km are used as fixed lower boundary conditions during the ideal MHD simulation. Open boundary conditions are imposed at the outer boundary, and finally reflective boundary conditions are set at the  $x$  and  $y$  boundaries of the simulation box.

Fig.7 shows the values of the radial component of the Lorentz Force at the lower boundary, the function  $\omega$  derived from the magnetic configuration and the resulting distribution of electron density  $n_e$  and temperature  $T$ . The Lorentz force is maximum at the location of the flux rope. The map of  $\omega$  follows the pattern we have prescribed, being higher around the region of the PIL and peaking where the flux rope is located. Consequently, the maps of  $n_e$  and  $T$  show the regions with a higher twisted magnetic field. In particular the position where the magnetic flux rope sits (compare with Fig.6) presents a density  $\sim 10$  times higher than its surroundings and a temperature value  $\sim 10$  times lower. It is also to be noted that in our model the location where the flux rope is relatively cold, is consistent with the observations of AIA in the 211Å band (Fig.6c) as

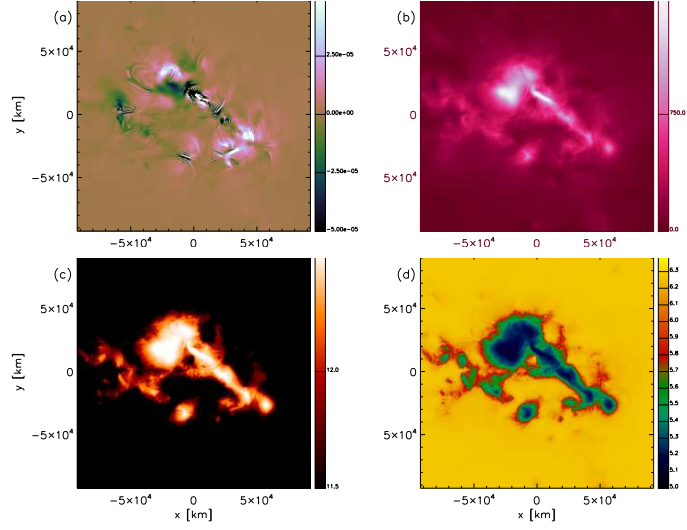


**Figure 7.** Lower boundary of the initial condition of the ideal MHD simulation: (a) Lorentz Force, (b)  $\omega$ , (c)  $\text{Log}_{10}(\rho[\text{g}/\text{cm}^3])$ , and  $\text{Log}_{10}(T[\text{K}])$ .

the location where the flux rope is not visible as the filter is tuned to observe plasma at higher temperatures.

The present initial conditions are clearly out of equilibrium for a number of reasons. In our simulation the initial plasma  $\beta$  ranges between the two extrema of  $\beta \sim 10^{-3}$  (at the flux ropes) and  $\beta \sim 10^3$  (in very confined regions where the magnetic field is less intense). Elsewhere it lies between  $10^{-2}$  and  $10^{-1}$ . Therefore, the strongest unbalanced force in the initial condition is the Lorentz force in the magnetic flux rope, directed upwards. At the same time, the radial profiles of density and pressure do not prescribe the balance between thermal pressure gradient and the gravity force. However, as addressed in detail in Pagano, Mackay, and Poedts (2013a), such unbalance shows effects over timescales longer than the dynamic triggered by the Lorentz force and therefore these can be neglected.

## 5. Results of the MHD simulation and comparison with observations

We run the MHD simulation starting from the final magnetic configuration obtained from the time series of NLFF fields when the magnetic flux rope is fully formed in order to describe the evolution of the ejection of the magnetic flux rope. As the initial conditions we derive are representative of the pre-eruptive magnetic configuration within a few minutes of indetermination, we present here the simulation evolution in terms of time elapsed from the initial condition and we let the observations to determine to which UT the initial condition corresponds. For this specific simulation, in Table 2 we report the onset of the eruption, thus time of the initial condition, at 05:54:40. The initial condition of the MHD simulation is out of equilibrium and several plasma flows occur at the beginning.

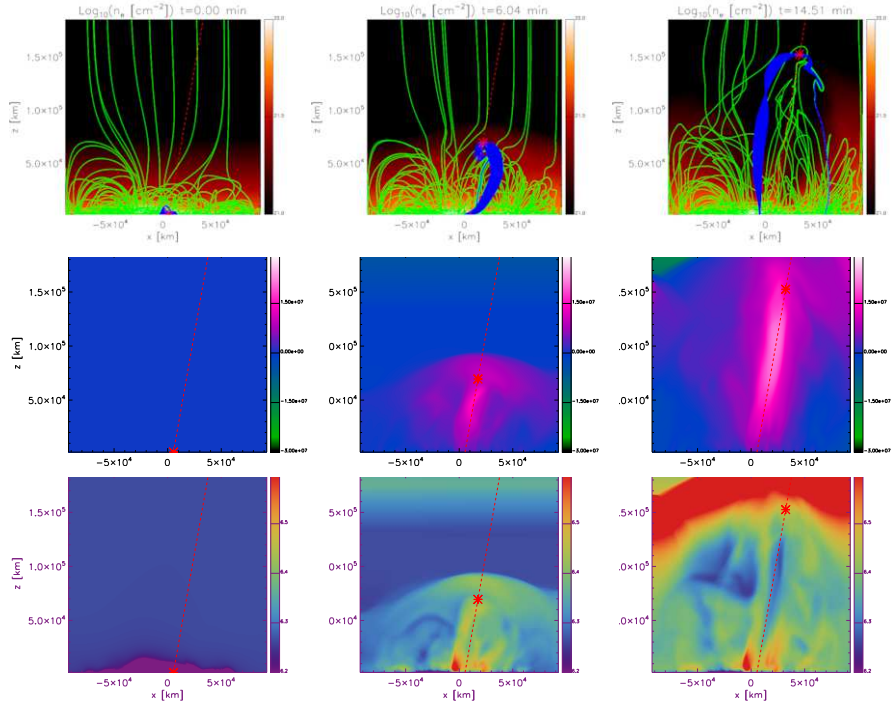


**Figure 8.** Panels showing quantities integrated along the  $y$  direction averaging by the electron density at different times. Upper row shows electron density, middle row  $z$ -component of the velocity, and lower row temperature. In the upper row, overplotted are some magnetic field lines (green lines) and magnetic field lines representative of the magnetic flux rope (blue lines). Left-hand side column shows quantities at the time in the simulation corresponding to  $t = 0$  min, central column to  $t = 6.04$  min, and right-hand side column to  $t = 14.51$  min. The red dashed line represent the direction of propagation of the magnetic flux rope and the red star on it is the position of the centre of the flux rope at each time.

However, the dominant evolution occur where the flux rope plasma is pushed upwards by the unbalanced Lorentz force and the flux rope starts erupting. In order to follow the evolution of the flux rope we display the simulation from a line of sight parallel to the  $y$  axis. In Fig.8 we show the electron density integrated along this line of sight, along with the temperature and velocity in the  $z$  direction integrated along the line of sight and weighted over  $n_e$ . We use as characteristic stages in the evolution the times of  $t = 0$  min,  $t = 6.04$  min, and  $t = 14.51$  min. Additionally, by considering the evolution of  $v_z$  and  $\omega$ , we manually track the directions of propagation of the magnetic flux rope and the position of its centre along this direction at each snapshot of the simulation. This is possible, because the cuts of both  $v_z$  and  $\omega$  along the direction of propagation of the flux rope show a local peak at the flux rope centre. This direction is represented by the red line and the position of the red star on it in Fig.8.

The particle density maps show an expansion and an upwards propagation of the structures that are initially lying low in the domain. The same motion is highlighted by the visible change in the magnetic field lines. In particular, the

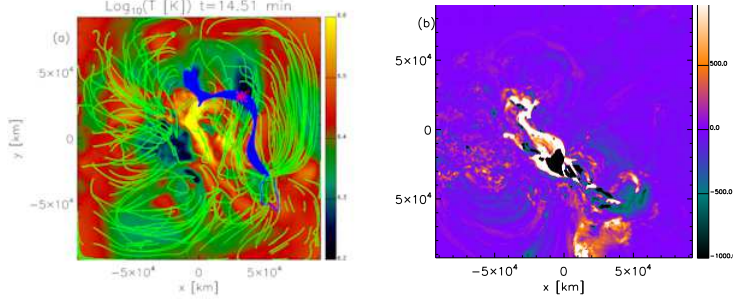


**Figure 9.** (a) Temperature integrated along the  $z$  direction averaging by the electron density at  $t = 14.51$  min in the MHD simulation. Overplotted are some magnetic field lines (green lines) and magnetic field lines representative of the magnetic flux rope (blue lines). (b) Difference in the AIA observations in the 211 Å passband between 06:09:00.62 and 05:55:00.62.

flux rope magnetic field lines (represented by the blue lines) show a distinctive motion, where the magnetic field lines are increasingly longer and less twisted over the evolution.

The evolution of  $v_z$  describes well this behaviour, where we see a region of upward directed velocity which is composed of an elongated region where the plasma velocity is higher and a bow-shaped region ahead that represents the front of the ejection. In particular, the elongated region extends along the direction of propagation of the flux rope, and dominates over other motions which are present in the domain. The maximum of  $v_z$  reaches values greater than 500 km/s at  $t = 11.5$  min in the MHD simulation. It should be noted that some boundary effects are visible at the external boundary, where some moderate inflow develops over the course of the simulation. However, the low density of the inflowing plasma makes this effect negligible for the dynamics of the ejection. It is interesting to notice that no shocks are formed ahead of the flux rope ejection. If we take into consideration the MHD simulation snapshot at 06:06:43 we find that the plasma speed at the front of the ejection is  $\sim 130$  km/s where the sound speed is  $\sim 300$  km/s. Only behind the propagation of the flux rope, we find regions with supersonic or superalfvenic velocities, where the Mach number is 1.5 or the Alfvénic mach number is  $\sim 3$ .

The evolution of temperature is significantly complex due to the energetics of the flux rope ejection. As already shown in similar simulations (Pagano, Mackay, and Poedts, 2014) the numerical resistivity plays a crucial role in heating the plasma, while expansion and decompression can lead to cooling of the plasma in certain regions. As soon as the simulation starts, magnetic energy is converted into thermal energy and this leads to an overall increase of the temperature. At the same time, this is not happening everywhere, but only where the magnetic field is initially more twisted, e.g. near the PIL. Subsequently, the temperature decreases in some regions, but it overall stays above the initial temperature.

Although the detailed comparison between the final state of the MHD simulation and the corresponding state in the region under study poses major challenges, it is still interesting to carry out a qualitative comparison to have a global understanding of the weaknesses and strengths of the model. Fig.9a

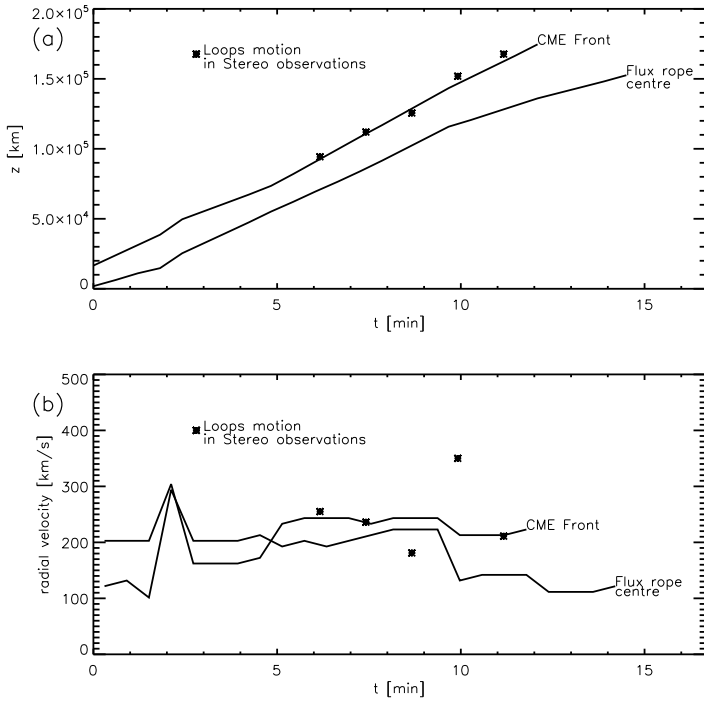


**Figure 10.** (a) Comparison between the position of the centre of the flux rope, the front of the flux rope ejection and the position of the upwards expanding loops in Stereo images as a function of time. (b) Comparison between the velocity of the centre of the flux rope, the velocity of the front of the flux rope ejection and the apparent velocity of the expanding loops in Stereo images as a function of time. Times are shown in seconds where 0 is the starting time of the MHD simulation at 06:00:41.

shows a map of the temperature averaged for the electron density along the line of sight from the top view at  $t = 14.51$  min in the MHD simulation. and Fig.9b shows a difference image between the AIA 211Å bass band at 06:09:00.62 and 05:55:00.62. The latter time is the closest AIA image to the assumed flux rope ejection time at 05:54:40, the former time is 14.3 minutes after, which is approximately the duration of the MHD simulation. We find that the region in the center of the field of view, where the emission in the AIA 211Å bass band is enhanced, roughly corresponds to a region in the MHD simulation where the plasma is heated up on average (to about 4 MK) and that a nearby location where the emission diminishes correspond to a relatively cold location in the MHD simulation. In general the MHD simulation shows an increase in temperature, which is consistent with the generally enhanced emission in the 211Å pass band. Also the magnetic field lines displayed in Fig.9a describe a topology with many similarities to the one suggested by the structures in Fig.9b. Examples include the system of loops in the left bottom corner of the field of view and the expanding structures on the top-right from the centre of the image. There roughly correspond to the flux rope location at this time in the MHD simulation.

Additionally, we have carried out a simple visual comparison of the kinematics of the flux rope ejection with STEREO observations taken over a time span after the observed start of the flux rope ejection (at 05:54:40 UT) corresponding to duration of the MHD simulation. The visual tracking of the CME in the STEREO images follows the apex of the expanding loops that initiate the CME motion (cross point in Fig.10a). In the same plot, these radial distances are compared with the tracked radial distance of the centre of the flux rope and the front that propagates from its ejection in the MHD simulation. We find a very good agreement of the locations identified in STEREO observations with the position of the front of the flux rope ejection, showing that probably the apex of the loops represents the motion of loops initially above the flux rope that starts to move as a consequence of being pushed by the ongoing ejection and represent their front. The same good agreement is found in Fig.10b where we compare the speeds of propagation of the flux rope and the front with the speed inferred from STEREO observations. In the MHD simulation, the CME front accelerates from  $100 \text{ km/s}$  to about  $200 \text{ km/s}$ , while the flux rope moves at  $200 \text{ km/s}$  until the end of the simulation where it slows down to  $100 \text{ km/s}$ . The points tracked in STEREO images always lie between  $150 - 350 \text{ km/s}$ . As we cannot consider this analysis further than a qualitative comparison, it is interesting to show that the velocity of the structure predicted by the MHD simulation is comparable with the speed at which the structures move in the STEREO observations. At the same time, it seems that the model underestimates the observed speed for at least a fraction of the time of evolution around  $t = 200 \text{ s}$ . There, the observed speed is  $\sim 1.5$  higher than the speed of the flux rope centre and front of the ejection in the MHD model. This difference would be enough to make the plasma flow overcome the sound speed and thus leading to a shock in the MHD model matching the observation. This may be a consequence of differences between the real atmospheric profile of  $\rho, T$  compared to the inferred and simulated one used here.

## 6. Ion charge state evolution of SW transients in the corona

Ion charge state of the CME plasma as well as its evolution in the corona depends mainly on the following factors: (i) chemical element to which considered ions belong, (ii) plasma conditions (such as temperatures and electron densities), and (iii) bulk velocities of plasma in the corona. In the previous sections we derived parameters of the erupting plasma and of the emerging flux rope at the distances up to  $0.25 R_{\text{sun}}$  from both direct EUV measurements and numerical simulations with the MHD model. In this section, we investigate the ion charge state evolution of the plasma structures under study by considering the ratios of carbon ( $\text{C}^{6+}/\text{C}^{5+}$ ) and oxygen ( $\text{O}^{7+}/\text{O}^{6+}$ ) and the average charge of iron ions ( $Q_{\text{Fe}}$ ), which were measured in-situ by ACE. For this purpose it is necessary to analyze how these parameters evolve during the plasma propagation in the corona at larger distances to several solar radii. We assume that in the whole space between the solar surface and the freeze-in region the expanding plasma is in a quasi-stationary state, i.e. the ionisation/recombination time scales are less than the expansion time scale of plasma.

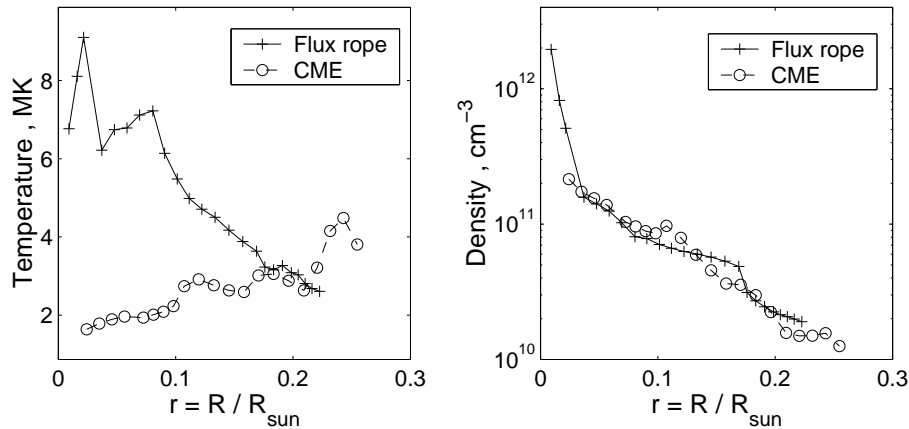


**Figure 11.** Evolution of electron temperature and density of the flux rope and CME plasma derived from the MHD simulations.

Evolution of the ion charge states in the corona can be described by the following system of the continuity equations for a set of ions from the atomic species of interest in the rest frame of the expanding plasma structure (see, e.g., Ko *et al.* (1997)):

$$\frac{\partial y_i}{\partial t} = N_e (y_{i-1} C_{i-1}(T_e) - y_i (C_i(T_e) + R_{i-1}(T_e)) + y_{i+1} R_i(T_e)) , \quad (17)$$

where  $y_i = n_i / \sum_{i=0}^Z n_i$  is the relative fraction of the ion with the number density  $n_i$  in charge state  $i$ ,  $N_e$  is the electron density,  $T_e$  is the electron temperature,  $C_i$  is the ionization rate coefficient for the transition from charge state  $i$  to  $i+1$ , and  $R_i$  is the total recombination rate (including both radiative and dielectronic recombination) from the charge state  $i+1$  to  $i$ . For integrating the system of equations (17) we used the recombination and ionization rate coefficients  $R_i$  and  $C_i$  from the CHIANTI database (Dere, 2007; Dere *et al.*, 2009) where these data are given on the assumption that the electron velocity distribution is Maxwellian.

In order to solve the system of equations (17), one needs to know the time evolution of electron density and temperature  $\{T_e(t), N_e(t)\}$  in a plasma structure under study as well as the bulk velocity of plasma,  $v(t)$ . Because the plasma parameters obtained from the EUV imaging and MHD modeling are known only in the low corona up to the distance  $r_0 \approx 0.25$  (in the units of  $R_{\text{sun}}$ ) from the solar surface, we model the evolution of plasma conditions at larger distances  $r > r_0$  analytically by taking into account the processes of cooling, heating, and expansion of the plasma and solve the system of Eqs. (17) for a chosen ion species. As initial conditions, we used the plasma parameters derived from the MHD simulations. The corresponding profiles of electron temperatures and densities for the flux rope and the emerging CME structure are presented in Figure 11.

The electron density at distances  $r > r_0$  is taken to have a power law form

$$N_e(r) = N_e(r_0) \left( \frac{r_0}{r} \right)^3, \quad (18)$$

which is consistent with the flux rope evolution for expansion in both length and radius (see, e.g., (Kumar and Rust, 1996; Lee *et al.*, 2009)). For the temperature profile we have used a form similar to the adiabatic relation

$$T_e(r) = T_e(r_0) \left( \frac{N_e(r)}{N_e(r_0)} \right)^\alpha, \quad (19)$$

where the power index  $\alpha$  is chosen to be consistent with in-situ measured values of ion composition parameters. In the case of the adiabatic expansion the factor  $\alpha = \gamma - 1$ , where  $\gamma = 5/3$  is the adiabatic index. This simple form of the temperature profile was used to account for possible heating, which the ejected plasma usually undergoes long after the eruption (see, e.g., (Akmal *et al.*, 2001; Ciaravella *et al.*, 2001)). Smaller values of the index  $\gamma$  are often used in coronal models to take phenomenologically into account heating mechanisms without a knowledge of heating rates (see also Kumar and Rust (1996); Lee *et al.* (2009)).

Using Eqs. (17), we have carried out calculations of ion charge state evolution of C, O, and Fe ions for the event on 2 August, 2011. A relationship between cooling rates of plasma by different mechanisms, such as the adiabatic expansion, thermal conductive cooling, and radiative losses, depends on the plasma parameters and configuration of the erupting structure and varies during the expansion in the corona. We analyzed and estimated the cooling effectiveness of these three terms separately for our plasma conditions by considering the temperature evolution of the flux rope and CME material. It was found that the most effective cooling factor is the adiabatic expansion. For instance, at the distance  $r = 0.5$  the fall of temperature for the adiabatic regime prevails those of the radiative and conductive cooling 3–5 times, and at  $r = 1$  up to one order of magnitude and more. Thus, it was shown that at distances  $r > 0.25$  the adiabatic expansion is the noticeably prevalent cooling process.

In assumption that cooling is provided elsewhere only by the adiabatic expansion, we obtained the following frozen-in ion composition parameters:  $C^{6+}/C^{5+} = 0.56$ ,  $O^{7+}/O^{6+} = 0.017$ ,  $Q_{Fe} = 7.4$  for the CME plasma, and  $C^{6+}/C^{5+} = 0.071$ ,  $O^{7+}/O^{6+} = 1.46 \cdot 10^{-4}$ ,  $Q_{Fe} = 7.4$  for the flux rope structure. These values are too low in comparison with the in-situ observations (see Table 3). If we then introduce a heating process in the whole space to the freeze-in region of Fe by decreasing the index  $\alpha$  from the adiabatic value  $2/3$  to  $0.1$ , the derived value of  $Q_{Fe}$  increases to  $\sim 10 - 11$ , which is in agreement with in-situ observations. However, in this case the ratios  $C^{6+}/C^{5+}$  and  $O^{7+}/O^{6+}$  become noticeably larger in 2–3 times in comparison with measurements.

In order to explain and to overcome this issue, we assumed that the heating power depends on the height in the corona. First, our numerical analysis showed that the ion charge states of C and O ions reach the freeze-in conditions at the distances of about  $1-2 R_{\text{sun}}$ , whereas the freeze-in region of Fe ions begins at the distances of  $\approx 4 - 5 R_{\text{sun}}$ . The reason is that the recombination time scales of carbon and oxygen ions,  $\tau_r = 1/(N_e R_i)$ , prevail those of iron ions.

Second, we considered separately two spatial intervals: the first one is from  $r_0$  to  $r_h = 1.5$  where the freeze-in conditions begin to play role only for C and O ions, and the second from  $1.5 R_{\text{sun}}$  to the Fe freeze-in region. We then calculated evolution of the ion charge states of C and O ions by matching the parameter  $\alpha$  so that to satisfy observational data in the first spatial interval. For the CME plasma we adopted the value  $\alpha = 0.35$  and found the frozen-in values equal to  $\text{C}^{6+}/\text{C}^{5+} = 2.2$  and  $\text{O}^{7+}/\text{O}^{6+} = 0.32$ . For the flux rope structure  $\alpha = 0.2$ , and  $\text{C}^{6+}/\text{C}^{5+} = 1.77$  and  $\text{O}^{7+}/\text{O}^{6+} = 0.14$ . At the same time, at  $1.5 R_{\text{sun}}$  we obtained  $Q_{\text{Fe}} \approx 7-8$ , which is noticeably lower than the measured in-situ values.

Using the functional temperature difference between the proper adiabatic expansion and the fitted values of the index  $\alpha$  for the CME plasma and flux rope, we also estimated the heating power from the coronal source which maintains this difference. It was found that this source acted from  $r_0$  to  $r \approx 0.5$  and its intensity sharply decreased with distance. The average heating power for the both plasma structures are  $Q_{\text{CME}} \approx 5 \cdot 10^{-3}$  [erg cm $^{-3}$  s $^{-1}$ ] for the CME and  $Q_{\text{FR}} \approx 6 \cdot 10^{-3}$  [erg cm $^{-3}$  s $^{-1}$ ] for the flux rope.

In order to match the value  $Q_{\text{Fe}}$  with the in-situ measurements, we assumed that in the second interval  $> 1.5 R_{\text{sun}}$  the parameter  $Q_{\text{Fe}}$  increased due to an additional heating power from the coronal source. We have taken the form of temperature evolution at distances  $r_h \geq 1.5$  as  $T_e(r) = T_h(r/r_h)^\beta$ . Taking the index  $\beta = 0.75$ , we obtained  $Q_{\text{Fe}} \approx 10$  for the CME structure and  $Q_{\text{Fe}} \approx 11$  for the flux rope, which is compatible with the in-situ observations. Our estimation of the heating power at the point  $r_h = 1.5$  gives  $Q_h \sim (1-2) \cdot 10^{-5}$  [erg cm $^{-3}$  s $^{-1}$ ].

## 7. Discussion

In our study we made an attempt to predict the ion charge state of the ICME produced by the flare/CME solar event on 2011 August 2, using the SDO/AIA EUV observations, MHD numerical simulation of the flux rope formation and analytical consideration of the plasma ion charge state evolution in the corona up to the freeze-in region. In our analysis we assume that ion composition of the ICMEs do not vary in the heliosphere due to sufficiently larger ionization/recombination relaxation times in comparison with the expansion time on the condition of very low collisional rates. In order to obtain the values of the ion charge state ratios  $\text{C}^{6+}/\text{C}^{5+}$  and  $\text{O}^{7+}/\text{O}^{6+}$  and the average charge  $Q_{\text{Fe}}$  close to that measured in-situ, we had to introduce a heating process which had different rates at the distances  $0.25-1.5 R_{\text{sun}}$  and  $1.5-5 R_{\text{sun}}$ . The results of plasma diagnostics (see Section 3.2) and MHD simulations suggest that the erupting plasma is heated far from the flare region. Figure 5 shows the temperature dropping to  $\approx 1.5$  MK at the base of the ejected structure under consideration, whereas MHD calculations exhibit noticeably higher temperatures for the flux rope and CME plasma. The assumption on a heating source above the flare region is of course debatable, but there are a number of works where the authors performed MHD simulations and discussed various heating mechanisms in the CME plasma (see, e.g., Lee *et al.* (2009); Lynch *et al.* (2011)).

Reinard, Lynch, and Mulligan (2012) carried out a numerical simulation of ion composition for two ICMEs (magnetic clouds) detected by STEREO and ACE on 21–23 May 2007 using the Magnetohydrodynamics-on-A-Sphere (MAS) and ARCT ideal 2.5D MHD models described earlier by Lynch *et al.* (2011). Both models took into account field-aligned thermal conduction, radiative losses and coronal heating from the flare site during initiation and expansion of a flux rope in the corona up to the distances more than  $10 R_{\text{sun}}$ . As it follows from their results, the key question in prediction of the ICME ion composition by the numerical MHD modeling is a correct definition of the ratio between heating and cooling processes acting on the erupting plasma in the corona. In the both models described by Lynch *et al.* (2011) heating is introduced as the dominating factor not depending on real conditions in the source. Thus, they obtained that the slower CMEs become hotter than the faster ones, which contradicts with observations. In contrary, we use a 3D MHD model to determine the plasma parameters of ejecta on the very initial stage of the flux rope ejection and fit the results with the EUV measurements by selecting the initial parameters of the simulation.

Our consideration refers to the case when the ICME parameters correspond to the apex of a CME. Though, in some cases presence of the nearby coronal holes (CHs) producing high-speed streams can seriously influence appearance and parameters of an ICME near the Earth (Gopalswamy *et al.*, 2009a,b; Mohamed *et al.*, 2012; Mäkelä *et al.*, 2013; Wood *et al.*, 2012; Gopalswamy *et al.*, 2013). Interaction of a CME with high-speed stream from the nearby coronal hole can deflect the CME from the Sun-Earth line which results in shift the arrival time ahead or behind the time predicted by kinematic models, and can change other SW parameters. We suppose that the ion composition parameters in the collisionless heliosphere are not influenced by such interaction and can be used for the source identification, but these cases are worth to be specially studied.

It should be noted, that the used model is rather simplistic and idealized, so does not reproduce some important details of the CME formation such as laminar and turbulent features of the evolution visible in observations. Energy dissipation via electric resistivity, heat conduction, viscosity and radiation should be especially taken into consideration during the early phase of the evolution in the dense corona. The used ideal one fluid MHD approach has a limited applicability in the case of the observed small scale and fast variations. Moreover, the numerical ideal MHD modelling we have conducted in this work does not take into account terms in the energy equation that play a role in the coronal dynamics. Thermal conduction can be responsible to diffuse heat in the domain, even if Pagano *et al.* (2007) and Pagano, Mackay, and Poedts (2014) showed that it is largely inhibited inside the flux rope during CME propagation. Radiative losses are not likely to significantly cool down the plasma over such short time scales in this temperature range. Finally, a more accurate treatment for the effect of magnetic resistivity, thus on the amount of magnetic energy converted into heating, would require much higher spatial resolution.

## 8. Summary and Conclusion

We present a complex study of a series of the SW transients observed by ACE on 4 – 7 August 2011 and their solar origins flares and CMEs occurred on 2, 3 and 4 August 2011 in AR 11261 near the centre of the disk. These events produced two shocks with sheaths and two ICMEs of the MC type as it was identified by Richardson and Cane. The second shock appeared on 5 August at 17:51 followed with a sheath produced a geomagnetic storm with  $Dst = -115$  nT. Analysis of ion charge state of SW revealed three transients with enhanced temperature-dependent ratios  $C^6/C^5$ ,  $O^7/O^6$  and the mean charge of iron ions  $Q_{Fe}$ , which can be associated with hot plasma released in the coronal sources. The first transient coincided with the first ICME (Table 1), two others preceded the second ICME. The shift in time between transients 2, 3 and ICME 2, probably, may be caused by interaction between CME 2 and 3. Using simulations with the WSA-Enlil Cone model, it was found that the third CME of 4 August surpassed the second CME of 3 August at the distance from the Sun about 0.6 AU.

We studied in detail formation of the first CME of 2 August using the SDO/AIA images in 211 Å and numerical simulations by the NLFFF/MHD model. The images of the eruption structures in different SDO/AIA spectral channels were used for diagnostics of the outflow plasma by the DEM method. From observational data it was found that in the event of 2 August the temperature of outflow plasma during its visible expansion from 0.1 to  $0.13 R_{sun}$  decreased from 2.7 to 1.7 MK, the density - from  $1 \cdot 10^9$  to  $5 \cdot 10^8 cm^{-3}$ . These values are lower than those obtained by modeling for the apex and correspond to the legs of the eruption shell. It confirms that heating is more effective in the upper part of the expanding structure.

The initiation of the CME of 2 August 2011 was simulated numerically using a combination of the NLFF magnetic field extrapolation model with a 3D MHD model of expanding flux rope specially suited for the given case. The results of simulation were compared with the EUV measurements. It was shown that the general topology of the magnetic field matched the visible loop structure whereas the flux rope was formed along the PIL and was pushed upwards by the unbalanced Lorentz force. The maximal speed was below the sound speed of 300 km  $s^{-1}$ , thus, the model did not predict creation of shock wave ahead of the flux rope ejection, although the shock was seen in observations. The MHD simulation showed the temperature of  $\sim 4$  MK in the centre of the field of view which coincides with an enhancement of radiation in the 211 Å channel. In the relative time scale starting at the moment of the flux rope raise-up, the simulated height/time dependence of the CME front up to the heights of  $0.25 R_{sun}$  very well agrees with that observed by STEREO in 171 Å at the limb, the difference in velocity being within the measurement errors  $\pm 60$  km  $s^{-1}$ .

Based on the results of observations and numerical simulation, the ion composition of the CME 1 in the freeze-in region in the event of 2 August 2011 has been calculated with some assumptions about heating and cooling processes. The calculated values of the main temperature-related ion ratios and the mean charge of iron agree with that measured in-situ under the assumption that the expanding plasma was heated by an additional source, and the average heating

power decreased with height from  $\sim (5-6) \cdot 10^{-3}$  [erg cm $^{-3}$  s $^{-1}$ ] at  $r_h \approx 0.5 \div 1.5$  to  $\sim (1-2) \cdot 10^{-5}$  [erg cm $^{-3}$  s $^{-1}$ ] at  $r_h \approx 1.5 \div 5$ .

In conclusion, consideration of the ion composition of CMEs enables to disclose a relationship between parameters of the SW transients and properties of their solar origins which opens new possibilites to validate and improve the SW forecasting models.

**Acknowledgments** The authors are grateful to Jie Zhang and Nat Gopalswamy as the ISEST coordinators for supporting of our studies of coronal sources of ICMEs. We also thank Ian Richardson and Hilary Cane for their list of Near-Earth Interplanetary Coronal Mass Ejections<sup>6</sup>, CDAW Data Centre<sup>7</sup> and CACTus software package<sup>8</sup> which we used in our observations. The authors would like to thank the GOES, SDO/AIA and ACE research teams for their open data used in our study. The results used in this paper obtained from WSA-Enlil Cone and DBM models<sup>9</sup>. This project has received funding from the European Research Council (ERC) under the European Union's Horizon 2020 research and innovation programme (grant agreement No 647214). We acknowledge the use of the open source ([gitorious.org/amrvac](http://gitorious.org/amrvac)) MPI-AMRVAC software, relying on coding efforts from C. Xia, O. Porth, R. Keppens. The computational work for this paper was carried out on the joint STFC and SFC (SRIF) funded cluster at the University of St Andrews (Scotland, UK).

## References

Akmal, A., Raymond, J.C., Vourlidas, A., Thompson, B., Ciaravella, A., Ko, Y.-K., Uzzo, M., Wu, R.: 2001, SOHO Observations of a Coronal Mass Ejection. *Astrophys. J.* **553**, 922. DOI. ADS. [[Akmal01](#)]

Andrews, M.D.: 2003, A Search for CMEs Associated with Big Flares. *Solar Phys.* **218**, 261. DOI. ADS. [[andrews03](#)]

Arge, C.N., Pizzo, V.J.: 2000, Improvement in the prediction of solar wind conditions using near-real time solar magnetic field updates. *J. Geophys. Res.* **105**, 10465. DOI. ADS. [[arge00](#)]

Borgazzi, A., Lara, A., Echer, E., Alves, M.V.: 2009, Dynamics of coronal mass ejections in the interplanetary medium. *Astron. Astrophys.* **498**, 885. DOI. ADS. [[borg09](#)]

Brueckner, G.E., Howard, R.A., Koomen, M.J., Korendyke, C.M., Michels, D.J., Moses, J.D., Socker, D.G., Dere, K.P., Lamy, P.L., Llebaria, A., Bout, M.V., Schwenn, R., Simnett, G.M., Bedford, D.K., Eyles, C.J.: 1995, The Large Angle Spectroscopic Coronagraph (LASCO). *Solar Phys.* **162**, 357. DOI. ADS. [[brueckner95](#)]

Burlaga, L., Fitzpenreiter, R., Lepping, R., Ogilvie, K., Szabo, A., Lazarus, A., Steinberg, J., Gloeckler, G., Howard, R., Michels, D., Farrugia, C., Lin, R.P., Larson, D.E.: 1998, A magnetic cloud containing prominence material - January 1997. *J. Geophys. Res.* **103**, 277. DOI. ADS. [[burlaga98](#)]

Cargill, P.J.: 2004, On the Aerodynamic Drag Force Acting on Interplanetary Coronal Mass Ejections. *Solar Phys.* **221**, 135. DOI. ADS. [[cargill04](#)]

Cargill, P.J., Chen, J., Spicer, D.S., Zalesak, S.T.: 1996, Magnetohydrodynamic simulations of the motion of magnetic flux tubes through a magnetized plasma. *J. Geophys. Res.* **101**, 4855. DOI. ADS. [[cargill96](#)]

<sup>6</sup><http://www.srl.caltech.edu/ACE/ASC/DATA/level3/icmetable2.htm>

<sup>7</sup>[http://cdaw.gsfc.nasa.gov/CME\\_list/index.html](http://cdaw.gsfc.nasa.gov/CME_list/index.html)

<sup>8</sup><http://sidc.oma.be/cactus/>

<sup>9</sup><http://ccmc.gsfc.nasa.gov>,<http://heliowebather.net/>

---

Ciaravella, A., Raymond, J.C., Reale, F., Strachan, L., Peres, G.: 2001, 1997 December 12 Helical Coronal Mass Ejection. II. Density, Energy Estimates, and Hydrodynamics. *Astrophys. J.* **557**, 351. DOI. ADS. [[Ciaravella01](#)]

Dere, K.P.: 2007, Ionization rate coefficients for the elements hydrogen through zinc. *Astron. Astrophys.* **466**, 771. DOI. ADS. [[Dere2007](#)]

Dere, K.P., Landi, E., Young, P.R., Del Zanna, G., Landini, M., Mason, H.E.: 2009, CHIANTI - an atomic database for emission lines. IX. Ionization rates, recombination rates, ionization equilibria for the elements hydrogen through zinc and updated atomic data. *Astron. Astrophys.* **498**, 915. DOI. ADS. [[Dere2009](#)]

D'Huys, E., Seaton, D.B., Poedts, S., Berghmans, D.: 2014, Observational Characteristics of Coronal Mass Ejections without Low-coronal Signatures. *Astrophys. J.* **795**, 49. DOI. ADS. [[dhuys14](#)]

Feldman, U., Landi, E., Schwadron, N.A.: 2005, On the sources of fast and slow solar wind. *Journal of Geophysical Research (Space Physics)* **110**, A07109. DOI. ADS. [[feldman05](#)]

Fisk, L.A., Schwadron, N.A., Zurbuchen, T.H.: 1998, On the Slow Solar Wind. *Space Sci. Rev.* **86**, 51. DOI. ADS. [[fisk98](#)]

Gibb, G.P.S., Mackay, D.H., Green, L.M., Meyer, K.A.: 2014, Simulating the Formation of a Sigmoidal Flux Rope in AR10977 from SOHO/MDI Magnetograms. *Astrophys. J.* **782**, 71. DOI. ADS. [[gibb14](#)]

Gopalswamy, N., Lara, A., Lepping, R.P., Kaiser, M.L., Berdichevsky, D., St. Cyr, O.C.: 2000, Interplanetary acceleration of coronal mass ejections. *Geophys. Res. Lett.* **27**, 145. DOI. ADS. [[gopalswamy00](#)]

Gopalswamy, N., Nunes, S., Yashiro, S., Howard, R.A.: 2004, Variability of solar eruptions during cycle 23. *Advances in Space Research* **34**, 391. DOI. ADS. [[gopals04](#)]

Gopalswamy, N., Mäkelä, P., Xie, H., Akiyama, S., Yashiro, S.: 2009a, CME interactions with coronal holes and their interplanetary consequences. *Journal of Geophysical Research (Space Physics)* **114**, A00A22. DOI. ADS. [[Gopals09a](#)]

Gopalswamy, N., Mäkelä, P., Xie, H., Akiyama, S., Yashiro, S.: 2009b, CME interactions with coronal holes and their interplanetary consequences. *Journal of Geophysical Research (Space Physics)* **114**, A00A22. DOI. ADS. [[Gopals09b](#)]

Gopalswamy, N., Mäkelä, P., Xie, H., Yashiro, S.: 2013, Testing the empirical shock arrival model using quadrature observations. *Space Weather* **11**, 661. DOI. ADS. [[Gopals13](#)]

Goryaev, F.F., Parenti, S., Urnov, A.M., Oparin, S.N., Hochedez, J.-F., Reale, F.: 2010, An iterative method in a probabilistic approach to the spectral inverse problem. Differential emission measure from line spectra and broadband data. *Astron. Astrophys.* **523**, A44. DOI. ADS. [[goryaev10](#)]

Gosling, J.T.: 1990, Coronal mass ejections and magnetic flux ropes in interplanetary space. *Washington DC American Geophysical Union Geophysical Monograph Series* **58**, 343. ADS. [[gosling90](#)]

Gruesbeck, J.R., Lepri, S.T., Zurbuchen, T.H., Antiochos, S.K.: 2011, Constraints on Coronal Mass Ejection Evolution from in Situ Observations of Ionic Charge States. *Astrophys. J.* **730**, 103. DOI. ADS. [[Gruesbeck11](#)]

Howard, R.A., Moses, J.D., Vourlidas, A., Newmark, J.S., Socker, D.G., Plunkett, S.P., Kondryke, C.M., Cook, J.W., Hurley, A., Davila, J.M., Thompson, W.T., St Cyr, O.C., Mentzell, E., Mehalick, K., Lemen, J.R., Wuelser, J.P., Duncan, D.W., Tarbell, T.D., Wolfson, C.J., Moore, A., Harrison, R.A., Waltham, N.R., Lang, J., Davis, C.J., Eyles, C.J., Mapson-Menard, H., Simnett, G.M., Halain, J.P., Defise, J.M., Mazy, E., Rochus, P., Mercier, R., Ravet, M.F., Delmotte, F., Auchere, F., Delaboudiniere, J.P., Bothmer, V., Deutsch, W., Wang, D., Rich, N., Cooper, S., Stephens, V., Maahs, G., Baugh, R., McMullin, D., Carter, T.: 2008, Sun Earth Connection Coronal and Heliospheric Investigation (SECCHI). *Space Sci. Rev.* **136**, 67. DOI. ADS. [[howard08](#)]

Hundhausen, A.J., Gilbert, H.E., Bame, S.J.: 1968, Ionization State of the Interplanetary Plasma. *J. Geophys. Res.* **73**, 5485. DOI. [[hundhausen68](#)]

Jian, L.K., MacNeice, P.J., Taktakishvili, A., Odstrcil, D., Jackson, B., Yu, H.S., Riley, P., Sokolov, I.V., Evans, R.M.: 2015, Validation for solar wind prediction at Earth: Comparison of coronal and heliospheric models installed at the CCMC. *Space Weather* **13**, 316. DOI. [[jian15](#)]

Kilpua, E.K.J., Luhmann, J.G., Jian, L.K., Russell, C.T., Li, Y.: 2014, Why have geomagnetic storms been so weak during the recent solar minimum and the rising phase of cycle 24? *Journal of Atmospheric and Solar-Terrestrial Physics* **107**, 12. DOI. ADS. [[kilpua14](#)]

Klein, L.W., Burlaga, L.F.: 1982, Interplanetary magnetic clouds at 1 AU. *J. Geophys. Res.* **87**, 613. DOI. ADS. [klein82]

Ko, Y.-K., Fisk, L.A., Geiss, J., Gloeckler, G., Guhathakurta, M.: 1997, An Empirical Study of the Electron Temperature and Heavy Ion Velocities in the South Polar Coronal Hole. *Solar Phys.* **171**, 345. ADS. [Ko1997]

Koskinen, H.E.J., Huttunen, K.E.J.: 2006, Geoeffectivity of Coronal Mass Ejections. *Space Sci. Rev.* **124**, 169. DOI. ADS. [kosk06]

Kumar, A., Rust, D.M.: 1996, Interplanetary magnetic clouds, helicity conservation, and current-core flux-ropes. *J. Geophys. Res.* **101**, 15667. DOI. ADS. [Kumar96]

Lara, A., Borgazzi, A.I.: 2009, Dynamics of interplanetary CMEs and associated type II bursts. In: Gopalswamy, N., Webb, D.F. (eds.) *Universal Heliophysical Processes, IAU Symposium 257*, 287. DOI. ADS. [lara09]

Lee, J.-Y., Raymond, J.C., Ko, Y.-K., Kim, K.-S.: 2009, Three-Dimensional Structure and Energy Balance of a Coronal Mass Ejection. *Astrophys. J.* **692**, 1271. DOI. ADS. [Lee09]

Lemen, J.R., Title, A.M., Akin, D.J., Boerner, P.F., Chou, C., Drake, J.F., Duncan, D.W., Edwards, C.G., Friedlaender, F.M., Heyman, G.F., Hurlburt, N.E., Katz, N.L., Kushner, G.D., Levay, M., Lindgren, R.W., Mathur, D.P., McFeaters, E.L., Mitchell, S., Rehse, R.A., Schrijver, C.J., Springer, L.A., Stern, R.A., Tarbell, T.D., Wuelser, J.-P., Wolfson, C.J., Yanari, C., Bookbinder, J.A., Cheimets, P.N., Caldwell, D., Deluca, E.E., Gates, R., Golub, L., Park, S., Podgorski, W.A., Bush, R.I., Scherrer, P.H., Gummin, M.A., Smith, P., Auker, G., Jerram, P., Pool, P., Soufli, R., Windt, D.L., Beardsley, S., Clapp, M., Lang, J., Waltham, N.: 2012, The Atmospheric Imaging Assembly (AIA) on the Solar Dynamics Observatory (SDO). *Solar Phys.* **275**, 17. DOI. ADS. [lemen12]

Lepri, S.T., Laming, J.M., Rakowski, C.E., von Steiger, R.: 2012, Spatially Dependent Heating and Ionization in an ICME Observed by Both ACE and Ulysses. *Astrophys. J.* **760**, 105. DOI. ADS. [lepri12]

Lynch, B.J., Reinard, A.A., Mulligan, T., Reeves, K.K., Rakowski, C.E., Allred, J.C., Li, Y., Laming, J.M., MacNeice, P.J., Linker, J.A.: 2011, Ionic Composition Structure of Coronal Mass Ejections in Axisymmetric Magnetohydrodynamic Models. *Astrophys. J.* **740**, 112. DOI. ADS. [Lynch11]

Ma, S., Attrill, G.D.R., Golub, L., Lin, J.: 2010, Statistical Study of Coronal Mass Ejections With and Without Distinct Low Coronal Signatures. *Astrophys. J.* **722**, 289. DOI. ADS. [ma10]

Mackay, D.H., Green, L.M., van Ballegooijen, A.: 2011, Modeling the Dispersal of an Active Region: Quantifying Energy Input into the Corona. *Astrophys. J.* **729**, 97. DOI. ADS. [mackay11]

Mäkelä, P., Gopalswamy, N., Xie, H., Mohamed, A.A., Akiyama, S., Yashiro, S.: 2013, Coronal Hole Influence on the Observed Structure of Interplanetary CMEs. *Solar Phys.* **284**, 59. DOI. ADS. [Makela13]

Manoharan, P.K.: 2010, Ooty Interplanetary Scintillation - Remote-Sensing Observations and Analysis of Coronal Mass Ejections in the Heliosphere. *Solar Phys.* **265**, 137. DOI. ADS. [manoh10]

Mays, M.L., Taktakishvili, A., Pulkkinen, A., MacNeice, P.J., Rastätter, L., Odstrcil, D., Jian, L.K., Richardson, I.G., LaSota, J.A., Zheng, Y., Kuznetsova, M.M.: 2015, Ensemble Modeling of CMEs Using the WSA-ENLIL+Cone Model. *Solar Phys.* **290**, 1775. DOI. ADS. [mays15]

McNeice, P., Elliot, B., Acebal, A.: 2011, Validation of community models. *Space Weather* **9**, S10003. DOI. [mcneice11]

Mohamed, A.A., Gopalswamy, N., Yashiro, S., Akiyama, S., Mäkelä, P., Xie, H., Jung, H.: 2012, The relation between coronal holes and coronal mass ejections during the rise, maximum, and declining phases of Solar Cycle 23. *Journal of Geophysical Research (Space Physics)* **117**, A01103. DOI. ADS. [Mohamed12]

Munro, R.H., Gosling, J.T., Hildner, E., MacQueen, R.M., Poland, A.I., Ross, C.L.: 1979, The association of coronal mass ejection transients with other forms of solar activity. *Solar Phys.* **61**, 201. DOI. ADS. [munro79]

Nolte, J.T., Roelof, E.C.: 1973, Large-Scale Structure of the Interplanetary Medium, I: High Coronal Source Longitude of the Quiet-Time Solar Wind. *Solar Phys.* **33**, 241. DOI. ADS. [nolte73a]

Odstrcil, D.: 1994, Interactions of solar wind streams and related small structures. *J. Geophys. Res.* **99**, 17. DOI. ADS. [odstril94]

---

Odstrčil, D., Pizzo, V.J.: 1999, Three-dimensional propagation of CMEs in a structured solar wind flow: 1. CME launched within the streamer belt. *J. Geophys. Res.* **104**, 483. DOI. ADS. [\[odstril99\]](#)

Odstrčil, D., Dryer, M., Smith, Z.: 1996, Propagation of an interplanetary shock along the heliospheric plasma sheet. *J. Geophys. Res.* **101**, 19973. DOI. ADS. [\[odstril96\]](#)

Owens, M., Cargill, P.: 2004, Predictions of the arrival time of Coronal Mass Ejections at 1AU: an analysis of the causes of errors. *Annales Geophysicae* **22**, 661. DOI. ADS. [\[owens04\]](#)

Pagano, P., Mackay, D.H., Poedts, S.: 2013a, Effect of gravitational stratification on the propagation of a CME. *Astron. Astrophys.* **560**, A38. DOI. ADS. [\[pagano13b\]](#)

Pagano, P., Mackay, D.H., Poedts, S.: 2013b, Magnetohydrodynamic simulations of the ejection of a magnetic flux rope. *Astron. Astrophys.* **554**, A77. DOI. ADS. [\[pagano13a\]](#)

Pagano, P., Mackay, D.H., Poedts, S.: 2014, Simulating AIA observations of a flux rope ejection. *Astron. Astrophys.* **568**, A120. DOI. ADS. [\[pagano14\]](#)

Pagano, P., Reale, F., Orlando, S., Peres, G.: 2007, MHD evolution of a fragment of a CME core in the outer solar corona. *Astron. Astrophys.* **464**, 753. DOI. ADS. [\[pagano07\]](#)

Pagano, P., Raymond, J.C., Reale, F., Orlando, S.: 2008, Modeling magnetohydrodynamics and non-equilibrium SoHO/UVCS line emission of CME shocks. *Astron. Astrophys.* **481**, 835. DOI. ADS. [\[Pagano08\]](#)

Pizzo, V., Millward, G., Parsons, A., Biesecker, D., Hill, S., Odstrcil, D.: 2011, Wang-Sheeley-Arege-ENLIL cone model transitions to operations. *Space Weather* **9**, S033004. DOI. [\[pizzo11\]](#)

Porth, O., Xia, C., Hendrix, T., Moschou, S.P., Keppens, R.: 2014, MPI-AMRVAC for Solar and Astrophysics. *Astrophys. J. Supplement Series* **214**, 4. DOI. ADS. [\[porth14\]](#)

Reinard, A.A., Lynch, B.J., Mulligan, T.: 2012, Composition Structure of Interplanetary Coronal Mass Ejections From Multispacecraft Observations, Modeling, and Comparison with Numerical Simulations. *Astrophys. J.* **761**, 175. DOI. ADS. [\[Reinard12\]](#)

Richardson, I.G., Cane, H.V.: 2004, The fraction of interplanetary coronal mass ejections that are magnetic clouds: Evidence for a solar cycle variation. *Geophys. Res. Lett.* **31**, L18804. DOI. ADS. [\[rich04\]](#)

Richardson, I.G., Cane, H.V.: 2010, Near-Earth Interplanetary Coronal Mass Ejections During Solar Cycle 23 (1996 - 2009): Catalog and Summary of Properties. *Solar Phys.* **264**, 189. DOI. ADS. [\[rich10\]](#)

Robbrecht, E., Patsourakos, S., Vourlidas, A.: 2009, No Trace Left Behind: STEREO Observation of a Coronal Mass Ejection Without Low Coronal Signatures. *Astrophys. J.* **701**, 283. DOI. ADS. [\[robb09\]](#)

Schou, J., Scherrer, P.H., Bush, R.I., Wachter, R., Couvidat, S., Rabello-Soares, M.C., Bogart, R.S., Hoeksema, J.T., Liu, Y., Duvall, T.L., Akin, D.J., Allard, B.A., Miles, J.W., Rairden, R., Shine, R.A., Tarbell, T.D., Title, A.M., Wolfson, C.J., Elmores, D.F., Norton, A.A., Tomczyk, S.: 2012, Design and Ground Calibration of the Helioseismic and Magnetic Imager (HMI) Instrument on the Solar Dynamics Observatory (SDO). *Solar Phys.* **275**, 229. DOI. ADS. [\[schou12\]](#)

Shi, T., Wang, Y., Wan, L., Cheng, X., Ding, M., Zhang, J.: 2015, Predicting the Arrival Time of Coronal Mass Ejections with the Graduated Cylindrical Shell and Drag Force Model. *Astrophys. J.* **806**, 271. DOI. ADS. [\[shi15\]](#)

Stone, E.C., Frandsen, A.M., Mewaldt, R.A., Christian, E.R., Margolies, D., Ormes, J.F., Snow, F.: 1998, The Advanced Composition Explorer. *Space Sci. Rev.* **86**, 1. DOI. ADS. [\[stone98\]](#)

Urnov, A.M., Goryaev, F., Oparin, S.: 2012, In: Shevelko, V., Tawara, H. (eds.) *On Spectroscopic Diagnostics of Hot Optically Thin Plasmas*, 249. DOI. ADS. [\[urnov12\]](#)

Urnov, A.M., Goryaev, F.F., Bertschinger, G., Kunze, H.J., Marchuk, O.: 2007, On the verification of atomic data for  $K$  radiation spectra from the TEXTOR tokamak. *Jetp Lett.* **85**, 374. DOI. [\[urnov07\]](#)

Vršnak, B.: 2001, Deceleration of Coronal Mass Ejections. *Solar Phys.* **202**, 173. DOI. ADS. [\[vrsnak01\]](#)

Vršnak, B., Žic, T.: 2007, Transit times of interplanetary coronal mass ejections and the solar wind speed. *Astron. Astrophys.* **472**, 937. DOI. ADS. [\[vrsnak07\]](#)

Vršnak, B., Vrbanec, D., Čalogović, J.: 2008, Dynamics of coronal mass ejections. The mass-scaling of the aerodynamic drag. *Astron. Astrophys.* **490**, 811. DOI. ADS. [\[vrsnak08\]](#)

Vršnak, B., Ruždjak, D., Sudar, D., Gopalswamy, N.: 2004, Kinematics of coronal mass ejections between 2 and 30 solar radii. What can be learned about forces governing the eruption? *Astron. Astrophys.* **423**, 717. DOI. ADS. [\[vrsnak04\]](#)

Vršnak, B., Žic, T., Falkenberg, T.V., Möstl, C., Vennerstrom, S., Vrbanec, D.: 2010, The role of aerodynamic drag in propagation of interplanetary coronal mass ejections. *Astron. Astrophys.* **512**, A43. DOI. ADS. [[vrsnak10](#)]

Vršnak, B., Žic, T., Vrbanec, D., Temmer, M., Rollett, T., Möstl, C., Veronig, A., Čalogović, J., Dumbović, M., Lulić, S., Moon, Y.-J., Shanmugaraju, A.: 2013, Propagation of Interplanetary Coronal Mass Ejections: The Drag-Based Model. *Solar Phys.* **285**, 295. DOI. ADS. [[vrsnak13](#)]

Wang, Y.-M.: 2012, Semiempirical Models of the Slow and Fast Solar Wind. *Space Sci. Rev.* **172**, 123. DOI. ADS. [[wang12](#)]

Webb, D.F., Howard, R.A.: 1994, The solar cycle variation of coronal mass ejections and the solar wind mass flux. *J. Geophys. Res.* **99**, 4201. DOI. ADS. [[webb94](#)]

Webb, D.F., Howard, T.A.: 2012, Coronal Mass Ejections: Observations. *Living Reviews in Solar Physics* **9**. DOI. ADS. [[fwebb12](#)]

Wood, B.E., Wu, C.-C., Rouillard, A.P., Howard, R.A., Socker, D.G.: 2012, A Coronal Hole's Effects on Coronal Mass Ejection Shock Morphology in the Inner Heliosphere. *Astrophys. J.* **755**, 43. DOI. ADS. [[Wood12](#)]

Yashiro, S., Gopalswamy, N.: 2009, Statistical relationship between solar flares and coronal mass ejections. In: Gopalswamy, N., Webb, D.F. (eds.) *Universal Heliophysical Processes, IAU Symposium* **257**, 233. DOI. ADS. [[yashiro09](#)]

Yermolaev, Y.I., Lodkina, I.G., Nikolaeva, N.S., Yermolaev, M.Y.: 2014, Influence of the interplanetary driver type on the durations of the main and recovery phases of magnetic storms. *Journal of Geophysical Research (Space Physics)* **119**, 8126. DOI. ADS. [[yerm14](#)]

Yigit, E., Frey, H.U., Moldwin, M.B., Immel, T.J., Ridley, A.J.: 2016, Hemispheric differences in the response of the upper atmosphere to the August 2011 geomagnetic storm: A simulation study. *Journal of Atmospheric and Solar-Terrestrial Physics* **141**, 13. DOI. ADS. [[yigit16](#)]

Zhang, J., Richardson, I.G., Webb, D.F., Gopalswamy, N., Huttunen, E., Kasper, J.C., Nitta, N.V., Poomvises, W., Thompson, B.J., Wu, C.-C., Yashiro, S., Zhukov, A.N.: 2007, Solar and interplanetary sources of major geomagnetic storms ( $Dst <-100$  nT) during 1996-2005. *Journal of Geophysical Research (Space Physics)* **112**, A10102. DOI. ADS. [[zhang07](#)]

Zhao, L., Zurbuchen, T.H., Fisk, L.A.: 2009, Global distribution of the solar wind during solar cycle 23: ACE observations. *Geophys. Res. Lett.* **36**, L14104. DOI. ADS. [[zhao09](#)]

Zhao, L., Landi, E., Zurbuchen, T.H., Fisk, L.A., Lepri, S.T.: 2014, The Evolution of 1 AU Equatorial Solar Wind and its Association with the Morphology of the Heliospheric Current Sheet from Solar Cycles 23 to 24. *Astrophys. J.* **793**, 44. DOI. ADS. [[zhao14](#)]

Zurbuchen, T.H., Richardson, I.G.: 2006, In-Situ Solar Wind and Magnetic Field Signatures of Interplanetary Coronal Mass Ejections. *Space Sci. Rev.* **123**, 31. DOI. ADS. [[zurbuchen06](#)]